Astronomy & Astrophysics manuscript no. output
April 14, 2026
©ESO 2026

Is the nitrogen-rich source PN K4-47 a true planetary nebula?

T. Steinmetz[1], T. Kamiński[1], D. Jones[2,3], M. Hajduk[4], D. R. Gonçalves[5], and S. Akras[6]

[1] Nicolaus Copernicus Astronomical Center, ul. Rabiańska 8, 87-100 Toruń, Poland e-mail: thomas@ncac.torun.pl
[2] Instituto de Astrofísica de Canarias, E-38205 La Laguna, Tenerife, Spain
[3] Departamento de Astrofísica, Universidad de La Laguna, E-38206 La Laguna, Tenerife, Spain
[4] Department of Geodesy, Faculty of Geoengineering, University of Warmia and Mazury, ul. Oczapowskiego 2, 10-719 Olsztyn, Poland
[5] Observatório do Valongo, Universidade Federal do Rio de Janeiro, Ladeira Pedro Antonio 43, 20080-090 Rio de Janeiro, Brazil
[6] Institute for Astronomy, Astrophysics, Space Applications and Remote Sensing, National Observatory of Athens, GR 15236 Penteli, Greece

Received XXX, accepted YYY

ABSTRACT

Context. The object K4-47 is a young planetary nebula that exhibits low-ionisation structures in the form of two 'lobes'. The unusual chemistry of the nebula has raised questions about whether K4-47 is a true planetary nebula or if the origins are more exotic in nature.
Aims. We aim to investigate the spatially resolved structure of the nebula, including in the sub-millimetre, for the first time. We examined the kinematics, chemistry, and mass-loss history of the nebula and probed the stellar properties of the central system.
Methods. We used a combination of optical imaging and spectroscopy and sub-millimetre interferometry as well as archival radio interferometric data to study the kinematics and morphology of the nebula and the differences between the atomic and molecular gas phases.
Results. We found extended CO (2–1) emission towards the northern optical lobe, which shows a clear velocity gradient along the same position angle as the optical bipolar nebula. Comparing the elemental and isotopic abundances to model predictions, we estimate an upper limit of 6 kpc for the distance to K4-47. The source hosts a fast (∼350 km s^{-1}) atomic jet and a slower (∼50–60 km s^{-1}) molecular outflow that are spatially coincident. The outflow velocity implies an age of 336 ± 119 yr. Using atomic line diagnostics, we found that the core has an electron temperature and density of ≈20 kK and 2800 cm^{-3}, respectively. We derived a Zanstra effective temperature of 81 ± 2 kK for the central star. We also observed evidence of a significant circumstellar component in the line-of-sight extinction to the source. The progenitor mass of K4-47 is estimated to be 4–6 M$_\odot$, based on the comparisons of measured abundances with model predictions. The central white dwarf of K4-47 may have an approximate mass of 0.9–1.1 M$_\odot$, following the initial-final mass relation of white dwarfs. The released material in the nebula is dominated by neutral atomic gas.
Conclusions. The resolved molecular environment of K4-47 indicates that it was shaped by the asymmetric outflow now seen primarily in optical emission. The progenitor of K4-47 was likely an asymptotic giant branch (AGB) star, possibly a J-type carbon star. We also observed that shocks, possibly from the bipolar lobes passing through the circumstellar environment, may play a non-negligible role in the excitation of gas in the core instead of just in photoionisation. The analysis indicates that K4-47 is indeed a true, albeit peculiar, planetary nebula.

1. Introduction

Planetary nebulae (PNe) are one of the last evolutionary stages for stars with masses M ≤ 8 M$_\odot$, occurring after the asymptotic giant branch (AGB) phase. These objects show a wide variety of morphologies ranging from spherical to highly multi-polar (Balick & Frank 2002). It is now thought that binarity plays a key role in the formation of the most strongly axisymmetric structures (Jones & Boffin 2017), in particular via common envelope evolution (CEE; Ivanova et al. 2013).

Common envelope evolution can also lead to the formation of more extreme transients known as luminous red novae (LRNe), which are believed to result from the merger of two non-compact stars (Soker & Tylenda 2003). These sources are characterised by intermediate luminosity eruptions, often with multiple outburst peaks (Metzger & Pejcha 2017) and low effective temperatures (Tylenda 2005), which give rise to molecules and dust (Kamiński et al. 2018). In addition, LRNe also often display discs or tori (Kamiński et al. 2010; Kamiński et al. 2021) and bipolar structures (Kamiński et al. 2020; Mobeen et al. 2024; Steinmetz et al. 2024).

The young PN K4-47 (IRAS 04166+5611) (∼400–900 yr; Corradi et al. 2000) exhibits an abundance of carbon-bearing molecules (Edwards et al. 2014; Schmidt & Ziurys 2016, 2017a,b, 2019) and isotopic enrichment (Schmidt et al. 2018). Molecule-rich PNe are unusual, as the conditions surrounding the central stars of PNe do not support molecule survival. Indeed, few molecules other than CO and H_2 have commonly been detected in PNe (see Kimura et al. 2012, and references within). Optical imaging of K4-47 has revealed three distinct morphological components: a nebulous core and two lobes that appear to be shock dominated (Gonçalves et al. 2004; Akras et al. 2017) and feature low ionisation structures (LISs; Gonçalves et al. 2001). The lobes are also apparent in infrared H_2 emission arising from shocked gas at an excitation temperature of 1400–1700 K (Lumsden et al. 2001b; Akras et al. 2017).

The isotopic enrichment in K4-47 (Schmidt et al. 2018) also bears a strong similarity to the oldest known Galactic LRN, CK Vul (Kato 2003). CK Vul is believed to be a merger between a red giant branch (RGB) star and a helium white dwarf (WD) (Tylenda et al. 2024). It shows a bipolar structure in optical, infrared, and sub-millimetre emission (Shara et al. 1985; Tylenda et al. 2019; Kamiński et al. 2020) as well as a faint extended

Article published by EDP Sciences, to be cited as https://doi.org/10.1051/0004-6361/202659366

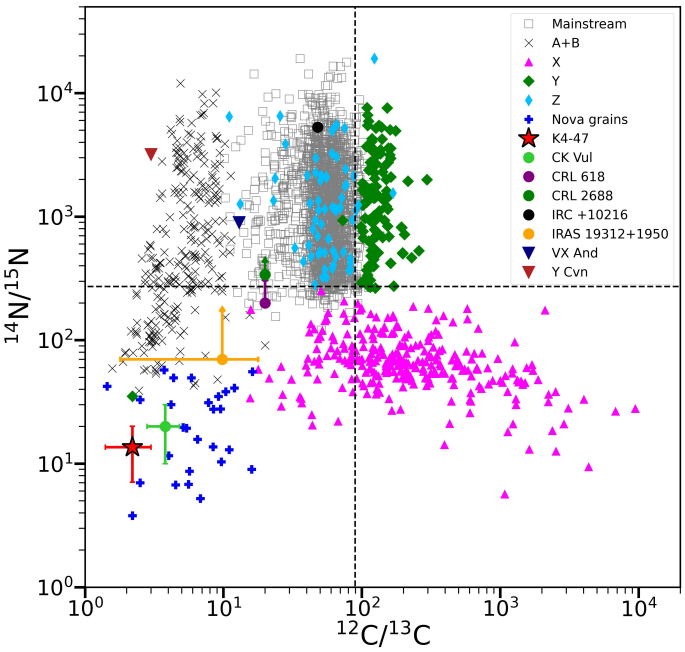

Fig. 1: Isotopic ratios of $^{12}C/^{13}C$ vs $^{14}N/^{15}N$ for different types of presolar SiC grains (Stephan et al. 2024). Included grains include mainstream; X, Y, and Z; A+B; and nova grains. Mainstream, Y, and Z grains are consistent with AGB stars of differing metallicities, X grains are thought to originate from core-collapse supernovae, and A+B grains originate from J-type stars (Liu et al. 2017). Also plotted are measured isotopic ratios for K4-47 (Schmidt et al. 2018) as well as the red nova CK Vul (Kamiński et al. 2017), the pre-PNe CRL 618, CRL 2688, the carbon-rich AGB star IRC +10216 (Wannier et al. 1991), the J-type carbon stars VX And, Y Cvn (Abia et al. 2017), and the peculiar unclassified source IRAS 19312+1950 (Qiu et al. 2023), which shows stellar properties associated with both young and evolved stars. The dashed black lines indicate Solar System values of the isotopic ratios (Lodders 2003).

hourglass nebula in Hα, which is reminiscent of many classical PNe (Hajduk et al. 2007). The similarity in isotopic enrichment, which is partially illustrated in Fig. 1, led Schmidt et al. (2018) to suggest that K4-47 may also be a stellar merger remnant.

In this paper, we examine this new potential origin of K4-47 and critically compare the properties of K4-47 and CK Vul in more detail using data across a wide range of wavelengths. Since only a few Galactic LRNe are known, identifying merger remnants at late epochs will help bring greater understanding of the evolution of these sources and produce better statistics on their properties. Such comparisons are key to identifying telltale signatures of red nova remnants years after the merger event as well as to avoiding misidentifications of both PNe and red novae. Additionally, by performing this comparison we also aim to better understand the nature of K4-47.

The paper is organised in the following sections. In Sect. 2 we describe the various observations in the optical, near-infrared (NIR), sub-millimetre, and radio. Section 3 presents the results, and in Sect. 4 we discuss the implications of the results, particularly for CK Vul. We summarise the paper in Sect. 5.

Table 1: ALFOSC observations.

Imaging					
Date	Filter	Central wavelength (Å)	FWHM (Å)	Exp. time (s)	Seeing (″)
21/09/97[1]	Hα	-	-	600	-
21/09/97	[N II]	-	-	600	-
22/10/97	[S II]	-	-	600	-
22/10/97	[O III]	-	-	600	-
27/11/24	Hα	6564	33	900	1.5
27/11/24	[N II]	6583	36	900	1.5
27/11/24	[S II]	6725	30	900	1.5
27/11/24	[O III]	5007	60	900	1.5
08/12/24	Hα	6564	33	900	0.6
08/12/24	[N II]	6583	36	900	0.6
08/12/24	[S II]	6725	30	900	0.6
08/12/24	[O III]	5007	60	900	0.6
26/02/25	Hα	6564	33	900	0.75
26/02/25	[S II]	6725	30	900	0.75
25/09/25	[O III]	5007	60	900	0.5
25/09/25	Hα	6583	36	900	0.5

Spectroscopy		
Date	Object	Exposure time (s)
08/12/24	K4-47	90
08/12/24	K4-47	900
08/12/24	Hiltner 600	60

Notes. [1]Central wavelength and FWHM for the 1997 observations are not known.

2. Observations

2.1. NOT

Narrowband imaging in Hα, [O III], [S II], and [N II] was obtained with the ALhambra Faint Object Spectrograph and Camera (ALFOSC) mounted on the 2.56m Nordic Optical Telescope (NOT) located at the Roque de los Muchachos Observatory on La Palma, at four different epochs: 27/11/2024, 08/12/2024, 26/02/2025, and 25/09/2025, under proposal 70-404 (PI T. Kamiński). We used the E2V 231-42 2k×2k CCD, which has a pixel size of 15.0 μm, equivalent to a plate scale of 0.″214/pixel across a 7.′3×7.′3 field of view (FoV). The detector used no binning with a readout time of 200 pixels/s. As well as these observations, archival data taken with ALFOSC in equivalent, but older, narrowband filters from 21/09/1997 and 22/10/1997 were obtained from the NOT archive. These observations were conducted using the older Loral 2k×2k detector. Detailed filter information for the filters used in 1997 is not currently available (see Table 1). K4-47 was also observed in Hα continuum in 1997, with an exposure time of 300 s, but K4-47 was not detected. All ALFOSC imaging data were calibrated using a combination of `ccdproc` v2.4.2[1] and `IRAF` routines. We performed astrometric calibration using the astrometry.net[2] web service, which identified field stars within the ALFOSC FoV and cross-matched them with star positions in public catalogues to build a new WCS for the images. This provided accurate WCS information with a precision of 0.″02–0.″05. We used the web service as there were only a few frames to calibrate. The ALFOSC observation details are shown in Table 1.

[1] https://ccdproc.readthedocs.io/en/2.4.2/
[2] https://nova.astrometry.net/upload

As well as imaging observations, we obtained an ALFOSC spectrum, with differing exposure times of 90 and 900 seconds, on 08/12/2024. The spectroscopic observation details are shown in Table 1. The spectra were taken using grism no. 7[3] and the horizontal slit with a width of 1″.0, giving a wavelength coverage of 3650–7100 Å. The resolving power R=650, giving an instrumental profile width of 461 km s^{-1}. The spectrum was corrected for bias and flat field using the IRAF package. The spectrum of Hiltner 600 was used to perform flux calibration, as well as a reference for the trace of K4-47. We extracted three separate spectra of K4-47 centred on the core, northern lobe, and southern lobe.

2.2. SMA

K4-47 was observed with the Submillimeter Array (SMA), located at Maunakea Observatory, Hawaii on 02/07/2019. The on-source time totalled 4.62 h, using the full range of 8 antennas placed in the sub-compact array with baselines between 4–58 m. We used a gain calibrator, 0359+509, and bandpass calibrator 3C 279. The data were calibrated in the IDL MIR environment[4]. The spectral setup covers four sub-bands within 210.15–280.64 GHz at a spectral resolution of 1.12 MHz. We reduced the data using the `TCLEAN` algorithm in CASA v6.4.1.2, with natural weighting and binned to a spectral resolution of 5 km s^{-1}. The spectrum was extracted from a region matching the most extended emission, in this case CO (2–1). Lines were identified using the Cologne Database for Molecular Spectroscopy (CDMS; Endres et al. 2016) and the Jet Propulsion Laboratory database (JPL; Pickett et al. 1998), available in the CASSIS spectroscopic analysis tool (Vastel et al. 2015); previous millimetre-wave studies (e.g. Edwards et al. 2014; Schmidt & Ziurys 2019) also assisted in line identification.

Our clean beam size at ~230 GHz (i.e. near CO 2–1) was 1″.51×1″.12 in natural weighting. This means that our SMA observations are the first to spatially resolve the molecular environment of K4-47 at millimetre wavelengths. We used the CASA routine `uvcontsub` to separate and subtract the continuum emission from the emission lines.

2.3. VLA

K4-47 was observed with the Karl G. Jansky Very Large Array (VLA) on 09/10/1983 at 4.86 GHz in array configuration A (PI: S. Kwok, project code AK94), using 25 antennas with baselines ranging between 25–350 m. Another dataset observed in 1984 as part of this project was published within Aaquist & Kwok (1990). The clean beam size for the VLA data were 0″.66×0″.40 at natural weighting, and the total integration time was 250 s. The data was extracted from the NRAO archive[5]. The original data was observed using FK4 coordinates, which were converted to FK5, using `astropy`.

3. Results

3.1. Optical imaging

Our images of Hα, [N II], and [S II] (Fig. 2) show the core and bipolar structures as previously seen by Corradi et al. (2000) and Gonçalves et al. (2004), with the core being only weakly detected in [S II]. The [O III] images, in contrast, only show the core emission. We used IRAF routines to combine all available epochs for each narrowband filter to create a single image per filter. This was done by normalising each epoch image to the mean of peak counts measured from five nearby stars seen in all ALFOSC images. Figure 2 shows the total Hα image, with contours from the total [N II], [S II], and [O III] images overlaid. The image shows that Hα and [N II] trace each other well spatially. The only slight difference between our ALFOSC images and those of Corradi et al. (2000) is that the latter detect clearer connecting emission in [S II] than seen in our data. This is likely due to observing conditions, rather than an evolutionary difference.

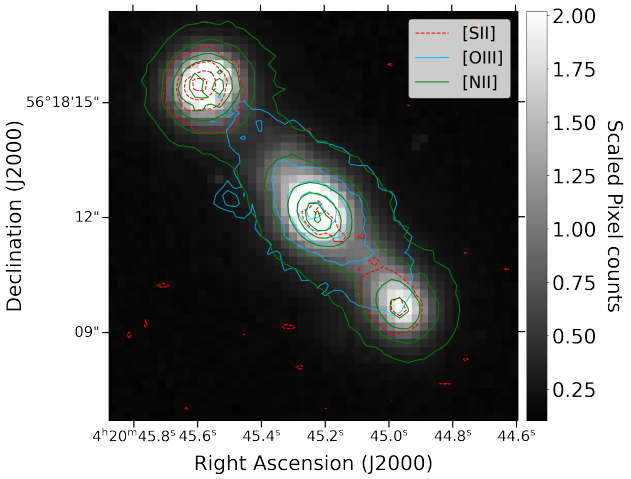

Fig. 2: Hα image combined over all epochs overlaid with contours at 20, 40, 60, 80, and 95% of the peak flux for [S II] (red) and [N II] (green). Contours representing [O III] are overlaid (blue) at 10, 20, 40, 60, 80, and 95% of the peak [O III] flux. The contours of the emission lines are from the images combined over all epochs.

To determine the expansion velocity of the lobes that dominate the nebula, we measured the centre of the 50% level contours of the maximum counts measured for the core and northern lobe in Hα for the 1997 and December 2024 epochs (shown in Fig. 3), which had the best seeing out of all available epochs. The 50% contour level was chosen as, at this level, we have distinct contours of both the northern lobe and the core. Assuming a distance of 5.9 kpc (Tajitsu & Tamura 1998), and an inclination angle to the observer of 67.5° (Corradi et al. 2000), we calculated the deprojected distance between the core and northern lobe for each epoch and calculate the expansion velocity. The measured angular distance change was 0.35″, from 4″.16 in September 1997 to 4″.52 in December 2024, which at a distance of 5.9 kpc gives a physical separation change from 2.45×10^4 AU in September 1997 to 2.67×10^4 AU in December 2024. The resulting deprojected expansion velocity is 382 ± 135 km s^{-1}. This is broadly consistent with the shock velocities of 250–300 km s^{-1} from Gonçalves et al. (2004). We then calculated the kinematical jet age of the optical bipolar outflow as 336 ± 119 yr, assuming constant velocity. The jet age is independent of distance, as both the projected length of the outflow and the outflow velocity are dependent on distance, and so the distance cancels out in the age calculation. This is comparable to the nebula age of 400–900 yr given by Corradi et al. (2000), assuming a distance range of 3–7 kpc.

[3] ALFOSC grism information can be found at https://www.not.iac.es/instruments/alfosc/grisms/
[4] https://lweb.cfa.harvard.edu/rtdc/SMAdata/process/mir/
[5] https://data.nrao.edu/portal/

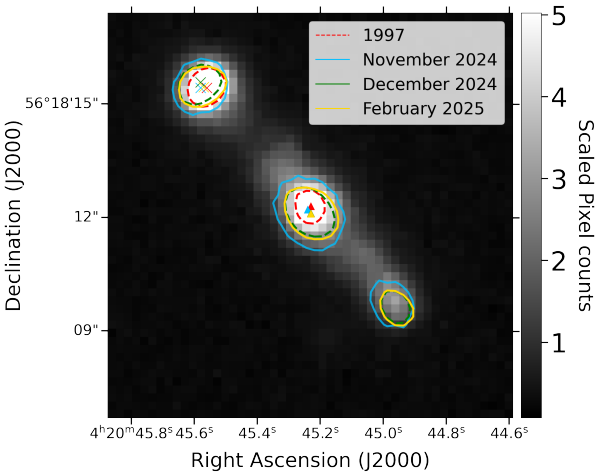

Fig. 3: Hα image from September 1997 with 50% contours overlaid for Hα from each epoch: September 1997 (red), November 2024 (blue), December 2024 (green), and February 2025 (yellow). The light-blue star symbol is located at the coordinates of K4-47, the triangles represent the fitted centre of the corresponding contours for the core, and the crosses show the centres of the corresponding contours for the northern lobe.

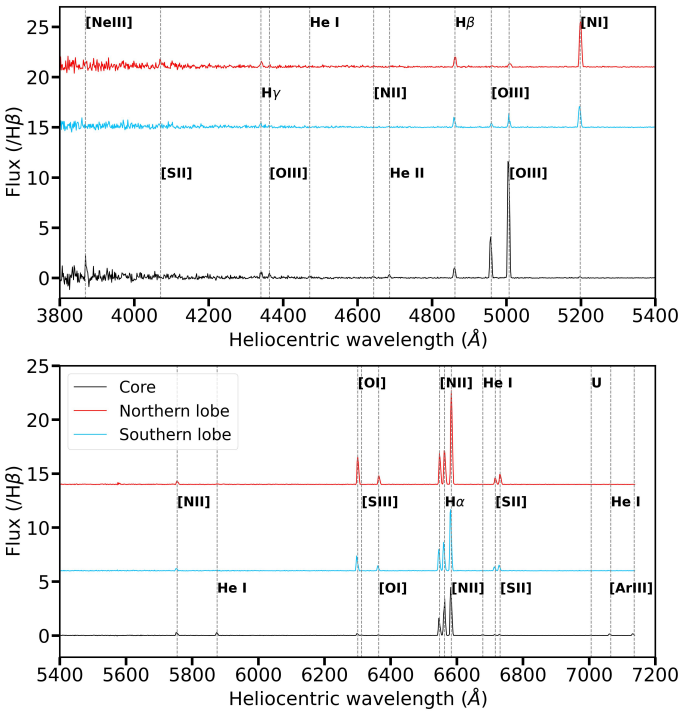

Fig. 4: Spectra extracted for each component of K4-47 (see text). Dashed grey lines and annotations indicate rest wavelengths of atomic lines seen in the spectrum.

3.2. Optical spectroscopy

In our optical ALFOSC spectra (Fig. 4), we detect a total of 24 atomic emission lines across the core and bipolar lobes. Many of these lines have been previously detected in K4-47 (Corradi et al. 2000; Gonçalves et al. 2004). The strongest lines in the core are the [O III]$\lambda\lambda$4959,5007 and [N II]$\lambda\lambda$6548,6584 doublets, as well as the Balmer Hα and Hβ lines. For the lobes, the [N II] doublet and Hα are the strongest, followed by [N I]λ5198 and [O I]λ6300, with the [O III] lines relatively weak compared to the core. [S II] is also much weaker in the core compared to the lobes. These differing line strengths are consistent with the distribution of the ionised atomic gas shown in Fig. 2, such as the [S II] emission found only in the lobes, but is mostly undetected in the core. We also include the tentative identification of the [Ar V]λ7005 line, detected at 7004.18 Å, which was identified by Henry et al. (2010). The tentative nature is marked with a '?' in Table A.1, as [Ar V] is usually expected in PNe with very hot central sources (e.g. NGC 7027, Wray 17-1, K1-2; Zhang et al. 2005; Akras & Gonçalves 2016), and the line could be instead [O I]λ7002. We favour the [Ar V] identification due to the previous identification in the literature, as well as the fact that [Ar V] would have a more consistent line velocity with other lines than [O I].

The range of measured line widths for the detected emission lines exceeds the instrumental broadening of 461 km s^{-1}. Therefore, no kinematical information could be extracted from our ALFOSC spectrum. Parameters of all detected lines are listed in Table A.1.

Reddening Gonçalves et al. (2004) identify significant interstellar extinction towards K4-47 across all three components ($C_{H\beta}$≈1.1–1.3, equivalent to E(B–V)=≈0.75–0.88 mag, following the extinction law of Cardelli et al. 1989, hereafter referred to as CCM89). Determining the physical properties of the central source in K4-47 is dependent on obtaining strong constraints of the reddening towards the source. To examine the reddening in our spectrum, we used the Balmer decrement

$$\mathrm{E(B-V)} = \frac{2.5}{\kappa(\mathrm{H}\beta) - \kappa(\mathrm{H}\alpha)} \quad \log_{10}\left(\frac{(\mathrm{H}\alpha/\mathrm{H}\beta)_{\mathrm{obs}}}{2.86}\right). \tag{1}$$

Here, $\kappa(\lambda)$ refers to the CCM89 extinction curve coefficient. The ratio Hα/Hβ is the flux ratio of the respective lines (see Table A.1). κ(Hβ) and κ(Hα) are taken to be 3.61 and 2.53, respectively, which are specific to the CCM89 extinction law. Our measured E(B–V) for the core, northern lobe, and southern lobe, are measured as 1.28 ± 0.01, 0.97 ± 0.01, and 0.76 ± 0.02 mag, respectively, using the measured Hβ and Hα fluxes for each component in our ALFOSC spectra (see Table A.1).

The extinction for the northern and southern lobes is consistent with the derived logarithmic extinction of Gonçalves et al. (2004). The northern lobe shows higher extinction than the southern lobe, which could be explained by the northern lobe being farther away from the observer and therefore may be located behind additional interstellar dust along the line of sight. However, the core shows the highest extinction of the three components. It is not clear if the increased extinction towards the core is only interstellar, or if there is a contribution from circumstellar dust. To test this, we used the GALEXTIN[6] VO service (Amôres et al. 2021) to examine the expected interstellar reddening in the direction of K4-47 based on multiple simulated dust maps. Our reddening analysis is described in Appendix E. We extracted interstellar reddening estimates for distances between 3–26.5 kpc (the range of distance estimates for K4-47: Aaquist & Kwok 1990; Cahn et al. 1992; van de Steene & Zijlstra 1994; Zhang 1995; Tajitsu & Tamura 1998; Corradi et al. 2000) for several dust maps (Amôres & Lépine 2005; Sale et al. 2014; Green et al. 2015, 2018, 2019). Most dust maps we examined predict ≈0.55–0.75 mag of interstellar extinction towards

[6] http://www.galextin.org/

K4-47, with model S from Amôres & Lépine (2005) predicting a value closer to 1.0 mag. The average range of extracted E(B–V) values from the dust models at the minimum and maximum distances are in the range of 0.62–0.75 mag, which represents the interstellar component of our measured value of E(B–V). The extinction towards the lobes are within 3σ of the interstellar extinction range predicted by the various dust maps, confirming the expected interstellar extinction contribution for K4-47. However, the extinction towards the core exceeds the dust maps' estimate. This means ~0.3–0.6 mag of the measured extinction is from circumstellar dust for the core of K4-47.

Temperatures and densities Despite the depth of literature on K4-47, there are no strong constraints on the central source properties of K4-47. The effective temperature (T_{eff}) of the central ionising source was previously estimated in the range of 115–130 kK by Gonçalves et al. (2004), using the Zanstra method. This method assumes photoionisation only, and neglects the effect of shocks. However, subsequent `CLOUDY` modelling using this value of T_{eff}, as well as the derived abundances lead to an underestimation of certain lines such as [O III]λ4363 and [N II]λ5755, which are frequently used to estimate the electron temperature. This discrepancy makes the derived abundances and T_{eff} uncertain, but remains the only estimate of the effective temperature for the central source in K4-47 to date. We first estimate T_{eff} of the central source using the relation between T_{eff} and the [O III]λ5007/Hβ ratio (see Lumsden et al. 2001a, their Fig. 7). From our dereddened spectrum for the core, we see that [O III]λ5007/Hβ = 11.74 ± 0.14. Using the blackbody models in Lumsden et al. (2001a), we get a range of T_{eff} ~ 60–90 kK. The implied value of T_{eff} from the linear fit to the Kaler & Jacoby (1991) data in the same figure is ~ 65 kK.

To estimate the electron temperature and density (T_e, n_e), we use the PyNeb emission line tool (Luridiana et al. 2015). We utilise the cross-convergence function `pyneb.Diagnostics.getCrossTemDen` to calculate the best-fitting electron T_e and n_e for emission line diagnostics. We use the forbidden line ratios of [N II]5755/6548 and 5755/6584, and [O III]4363/5007, which are all sensitive to electron temperature, and the electron density-sensitive forbidden line ratio [S II]6731/6716. We find that the diagnostics involving the [N II] ratios give electron temperatures exceeding 20000 K, which is the upper sensitivity limit for these lines (see Chapter 5 and Fig. 5.1 of Osterbrock & Ferland 2006). We therefore only use the results of the diagnostics of the [O III] and [S II] ratios, which gives T_e=19900 ± 1200 K and n_e=2800 ± 700 cm^{-3}. Our value of T_e is consistent with the [O III]-derived T_e (19900 K) of Mari et al. (2023). We then use these values, along with the He II λ4686/Hβ ratio, to derive the Zanstra temperature. We calculate the blackbody photon flux ratio Q(He$^+$)/Q(H$_0$) for a given T_{eff}, and calculate the observed photon flux ratio for our measured line fluxes, using Case B recombination coefficients of Storey & Hummer (1995), and find the minimisation between the difference of the theoretical and observed photon flux ratios using Brent's method. This method yields a Zanstra effective temperature for the central source of 81500 ± 1800 K.

Mass As shown in Table A.1, we detected multiple transitions from ionised atomic gas in all three morphological components. We calculated the ionised gas mass (M_{ion}) present in the core from

$$M_{ion} = \frac{m_p L_{H\alpha}}{h\nu_{H\alpha}\alpha^{eff}_{H\alpha} n_e}, \quad (2)$$

where m_p is the mass of a proton (1.67×10^{-27} kg), $L_{H\alpha}$ is the luminosity of the Hα line for the core, $\nu_{H\alpha}$ is the frequency of the Hα line, and $\alpha^{eff}_{H\alpha}$ is the effective recombination coefficient for Hα, which at T_e=19900 K is 6.31×10^{-14} cm^3 s^{-1} (Osterbrock & Ferland 2006). We calculate M_{ion} for full range of estimated distances from the literature (3–26.5 kpc). This gives a range of values for M_{ion} between 6.93×10^{-4}–5.21×10^{-2} M$_\odot$ for the core, 2.32×10^{-4}–1.74×10^{-2} M$_\odot$ for the northern lobe, and 9.65×10^{-5}–7.24×10^{-3} M$_\odot$ for the southern lobe. In Sect. 3.5, we provide distance constraints and the corresponding ionised masses.

3.3. SMA and H_2

Previous sub-millimetre and millimetre-wave studies of K4-47 (Huggins et al. 2005; Edwards et al. 2014; Schmidt & Ziurys 2016, 2017b,a; Schmidt et al. 2018; Schmidt & Ziurys 2019) have used single dish observations from facilities such as the IRAM 30m telescope, the Arizona Radio Observatory, and the Sub-Millimeter Telescope to detect various molecules in K4-47. In our SMA observations, which spatially resolved the molecular circumstellar medium (CSM) for the first time, we find emission of previously detected molecules such as CO, HC_3N, CCH, CN, and H_2CO. We also detect several isotopologue lines of detected molecules, including H^{13}CN, H^{13}CO$^+$, and ^{13}C^{17}O. All detected lines are listed in Table B.1. Our sensitivity was insufficient to detect several weak lines (e.g. of SiO) which were previously detected at the covered frequency range within the single-dish surveys. Using the CO (2–1) line, we used the CASA routine `imfit` to measure a beam-deconvolved source size of (2.″36±0.″10) × (1.″12±0.″08). Our SMA data were not adequate to perform any excitation analysis of the observed molecular emission, as we did not cover multiple transitions of the same molecular species. For source averaged line fluxes, this has been done in Schmidt & Ziurys (2019) and Edwards et al. (2014), where column densities for main species were derived. They also derived the hydrogen density of roughly 10^5–10^6 cm^{-3} and a temperature of 10–65 K. The SMA spectrum, re-binned to 20 km s^{-1} for better signal-to-noise ratio (S/N), is shown in Fig. 5.

To establish the molecular source morphology, we made integrated intensity maps of the detected lines. The exceptions were HC^{15}N and HCC^{13}CN, which are apparent in the spectrum, but no clear source was visible in the integrated flux maps. For the strongest lines (CO 2–1 and H^{13}CN 3–2), we also made velocity-field maps (moment-1 maps), where signal below the 3σ and 5σ noise level was clipped (see Table C.1).

We present the integrated flux maps in Figs. 6 and C.1 (with sigma clipping at 5σ and 3σ, respectively), and the integrated velocity maps in Fig. 7. The maps are shown with spatial offsets calculated relative to the peak position of the H^{13}CN emission, which is not optically thick or contaminated by multiple lines (unlike CO and CN, respectively). The majority of the emission shows an elongated structure compared to the continuum emission, with the exception of H^{13}CO$^+$ (3–2) and HN^{13}C (3–2), which shows a more compact distribution. The elongated structures span from the north-east to south-west at a similar PA to that seen in the optical and NIR H_2 maps (see Figs. 2 and 9). The elongation therefore appears to be, at least partially, shaped by the bipolar outflow seen in the optical images (Fig. 2). CO emission is seen to extend farther towards the northern lobe, forming

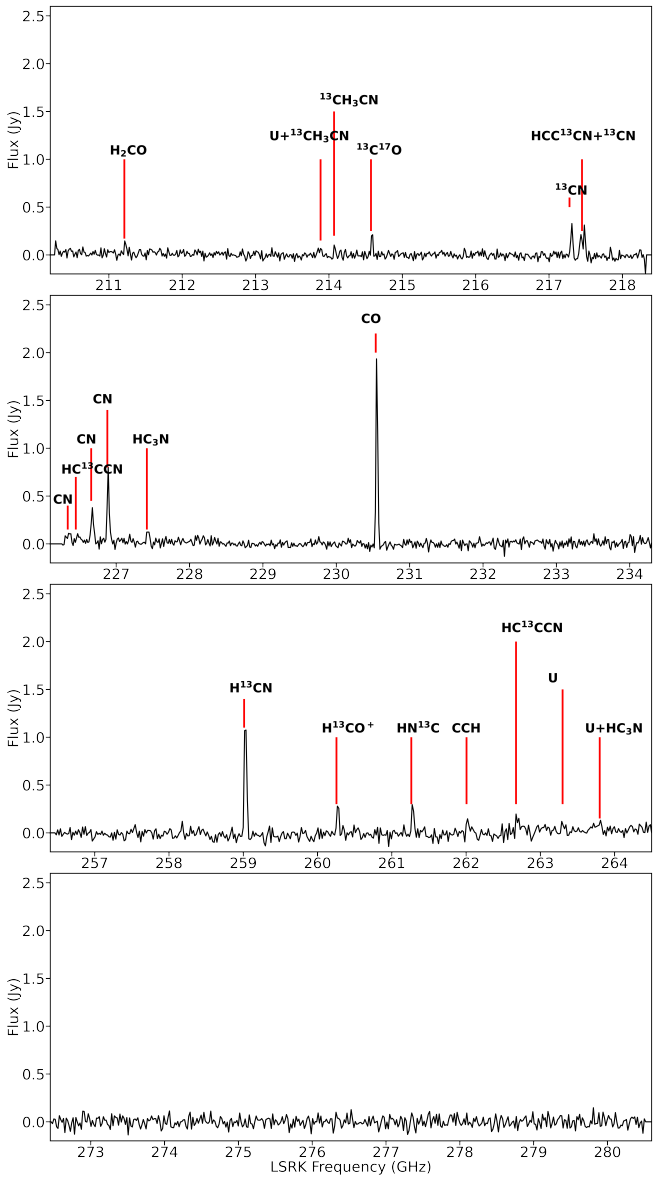

Fig. 5: Continuum-subtracted SMA spectrum of K4-47 after rebinning to 20 km s^{-1} for easier visual inspection. The spectrum is extracted from a region encompassing the entire CO (2–1) emission (see Fig. 6), i.e. the most extended molecular emission observed.

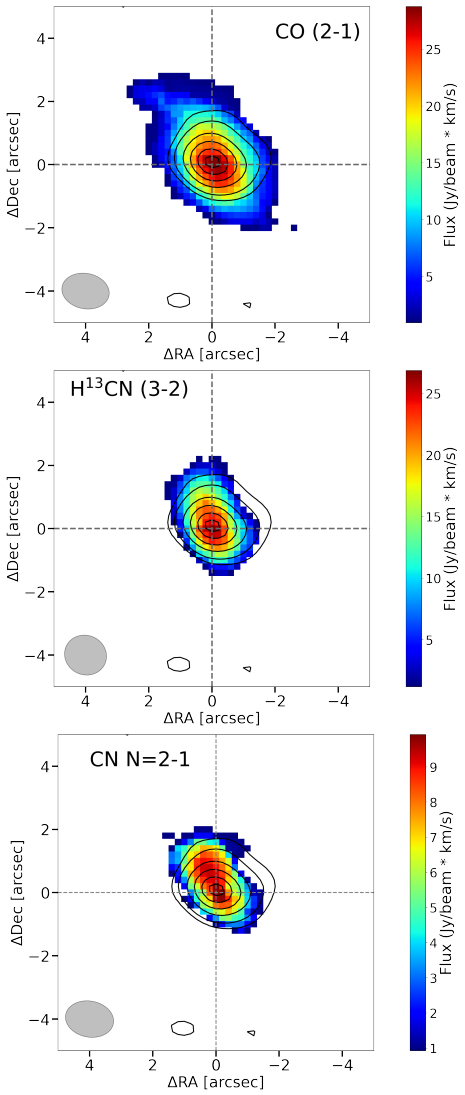

Fig. 6: Integrated flux maps of CO J=2–1 (left), H^{13}CN J=3–2 (centre), and CN N=2–1 (right). All maps have noise clipped at the 5σ level. Black contours are 10, 20, 40, 60, 80, and 95% of the peak continuum flux. The grey ellipse represents the synthesised beam for the molecular transition.

a bridge between the northern lobe and the core that is also seen in the optical images (see Fig. 9). The extended part of CO is also seen in the velocity maps of CO (Fig. 7), where the north-east tip of the CO emission suddenly changes velocity. The extent of the other strong lines (e.g. CN J=$\frac{5}{2}$–$\frac{3}{2}$ and H^{13}CN 3–2) is less than that for CO, and both extend to approximately half of the angular distance to the northern lobe. No such extension is seen towards the southern lobe. The integrated velocity maps for CO, CN, and H^{13}CN show that the northern lobe is redshifted, and the southern lobe is blueshifted. Using the moment-0 map of CO (2–1) shown in Fig. 6, we measured the CO flux in the core and northern lobe using a 2.″0 aperture. We found that the extended CO emission that overlaps partially with the northern lobe constitutes 8.7% of the core CO flux.

The CO (2–1) emission shows a velocity gradient along a PA of 41°. The H^{13}CN velocity map shows a similar structure at a PA of 13°. We made position-velocity (PV) diagrams of the CO (2–1) emission, at PA=41° (the PA of the atomic outflow; Gonçalves et al. 2004) and 131°, measured from north through east, using the CASA routine `impv`. These PV diagrams are shown in Fig. D.1. The PV diagram along the outflow PA shows a clear outflow structure in both directions, with the outflow on the southern side weaker than the north. The perpendicular PV diagram (PA=131°) shows no clear substructure.

Our SMA data use the local standard of rest (LSR) velocity rest frame. The maximum LSR velocity seen in the CO velocity map in the northern direction is 34.6 km s^{-1}, in the form of a high-velocity tip in the north-east part of the CO (2–1) velocity map (fig. 7). We estimated the CO 'systemic' velocity by taking the average velocity of the central CO region (neglecting the northern lobe and extended emission), and measuring the difference in velocity of the high-velocity tip and the central region. The central region's average velocity is –21.1 km s^{-1}, giving a molecular outflow velocity of 55.7 km s^{-1}. We measure the distance between the tip of the northern outflow and the central co-

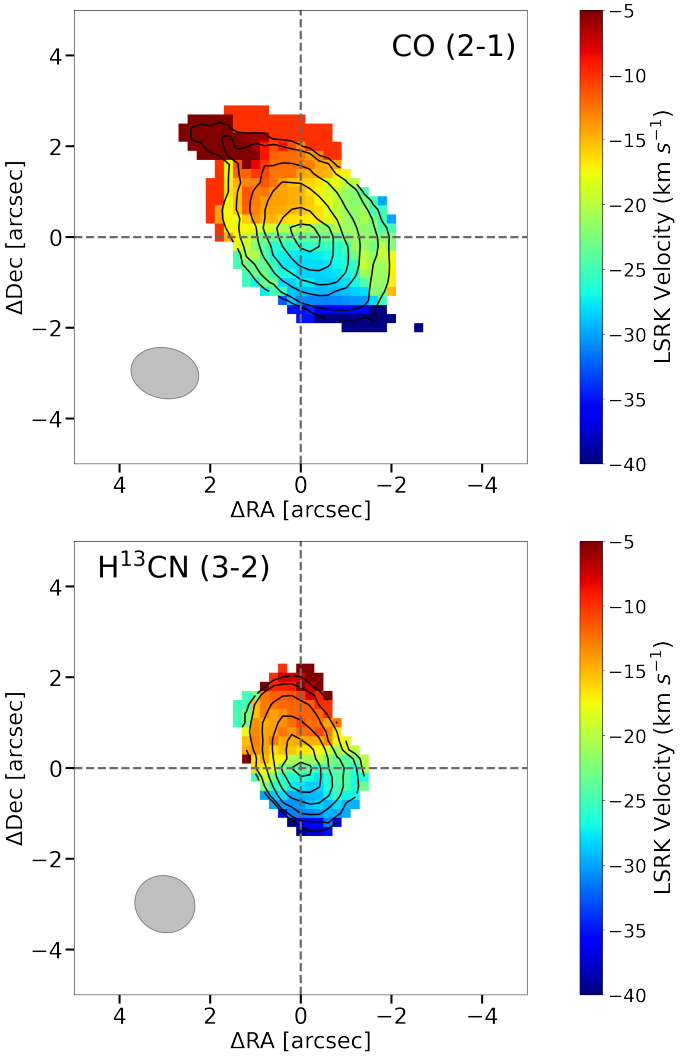

Fig. 7: Integrated velocity maps of CO (2–1) and $H^{13}CN$ (3–2). Dashed grey lines show the map centre, and grey ellipses show the synthesised beam for each emission line. For the CO map, the velocity range has been set to match that of $H^{13}CN$ for comparison, even though the maximum redshifted velocity exceeds this range.

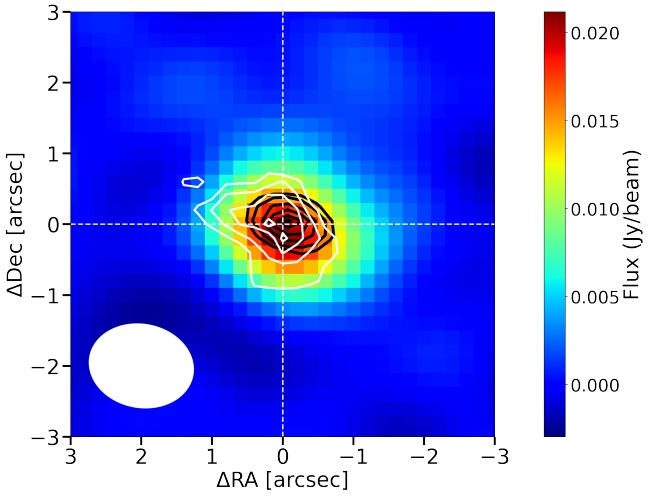

Fig. 8: Continuum image of K4-47 observed with SMA near 250 GHz. The black contours are 10, 20, 40, 60, 80, and 95% of the peak flux of the 1983 VLA observations at 5 GHz. The white contours are 40, 60, 80, and 95% of the peak of the SMA $^{13}C^{17}O$ integrated flux map (see Fig. C.1). The white ellipse indicates the SMA beam size.

ordinates (marked by the grey cross in Figs. 6 and 7) to be 3.″41. Using a distance of 5.9 kpc (Tajitsu & Tamura 1998) and an inclination angle i=67.°5 (Corradi et al. 2000), we get a deprojected distance of 0.10 pc. Assuming a constant velocity expansion, this gives us a dynamical timescale of 1740 yr for the molecular outflow. It is thus older than the optical outflow component (Sect. 3.1).

We also made a multi-frequency synthesis (mfs) image using `tclean` to show the continuum emission (Fig. 8). The continuum image displays a compact continuum source of comparable size to the radio source detected with VLA (Aaquist & Kwok 1990, see also Sect. 3.4), and no extended emission. The image was constructed using the entire spectral window between 272.6–280.5 GHz (Fig. 5, bottom panel), as well as continuum regions in other spectral windows absent of emission lines. The full range of frequencies used were between 211.2–280.5 GHz. The equivalent frequency of the continuum image is 246.46 GHz and the measured flux is 30.6±2.1 mJy. The central position of the continuum is α=04:20:45.2853, δ=+56:18:12.7790. Using `imfit`, we get a beam-deconvolved continuum source size of (1.″02±0.″57) × (0.″78±0.″53).

As well as sub-millimetre observations of molecules with SMA, we examine archival continuum-subtracted H_2 1–0 S(1) (λ=2.12 μm) observations from Akras et al. (2017), observed with Gemini North in the infrared. This was the only previously resolved observations of the molecular environment in K4-47. Akras et al. (2017) showed that the H_2 emission traces the shocked regions surrounding the outflow that gives rise to the lobes seen in optical emission, which represents the walls of the cavity produced by the outflowing material. The provided astrometry for the data from Gemini was inaccurate, resulting in us having to manually shift the astrometric solution by –1″ in declination. Typically, the infrared H_2 emission requires much higher excitation conditions than the molecules traced at millimetre wavelengths. Lumsden et al. (2001b) found excitation temperatures for the H_2 gas between 1600–1700 K, whilst Schmidt & Ziurys (2019) found an excitation temperature of 65 K for pure rotational lines of CO.

In Fig. 9, we compare the distribution of the CO (2–1) and H_2 emission to the Hα image combined over all epochs. The CO (2–1) distribution centre is offset by ~0.″5 north-east of the apparent centre of the Hα image, as is the H_2 distribution from Akras et al. (2017). The two molecular species do not overlap exactly in space, possibly due to different excitation conditions. Emission of molecular hydrogen does not overlap very well with Hα emission as well, except for the outer tips of the lobes, which are dominated by shock excitation.

Molecular line velocities and widths are presented in Table B.1. The central line velocities are in the range of –17 to –35 km s^{-1}, in contrast to the typical velocities of –27 to –28 km s^{-1} (Edwards et al. 2014; Schmidt & Ziurys 2016, 2017a,b, 2019), which were obtained with single dish (and therefore unresolved) sub-millimetre observations. $^{13}CH_3CN$ has a measured central velocity of –6 km s^{-1}, but this is likely affected by blending or low S/N. The discrepancy between our measurements and the literature is likely due to our modest S/N in the weaker analysed lines. The majority of molecular lines detected by Schmidt

& Ziurys (2019) have similar line widths, although we do not find any lines with the extended pedestal reported for CO (6–5) and HCO^+ (3–2) in Edwards et al. (2014), which indicates higher velocity emission. We did not cover any high-excitation lines such as CO (6–5), and while we covered $H^{13}CO^+$ (3–2), it may have a too low S/N to show the high velocity components. Much higher sensitivity is required to detect the high velocity component, which is expected to be spatially coincident with the lobe tips.

3.4. VLA

The compact 5 GHz radio source contours detected with VLA are shown, along with $^{13}C^{17}O$ (2–1) emission, both overplotted on the sub-millimetre continuum from SMA, in Fig. 8. The deconvolved source size is (208 ± 11) × (44 ± 22) mas, with PA=49.9 ± 4.0°, slightly off-axis from the optical bipolar lobes (PA=41°; Gonçalves et al. 2004). The radio emission is centred almost exactly on the SMA continuum peak (Fig. 8). The total integrated flux of the source is 5.75 ± 0.04 mJy, somewhat lower than the Aaquist & Kwok (1990) value of 7.7 mJy from 1984. Our source size is also smaller than that of Aaquist & Kwok, who obtained an angular size of 0″.25. The similar observation epochs mean that the discrepancy in radio flux is likely not a consequence of source evolution.

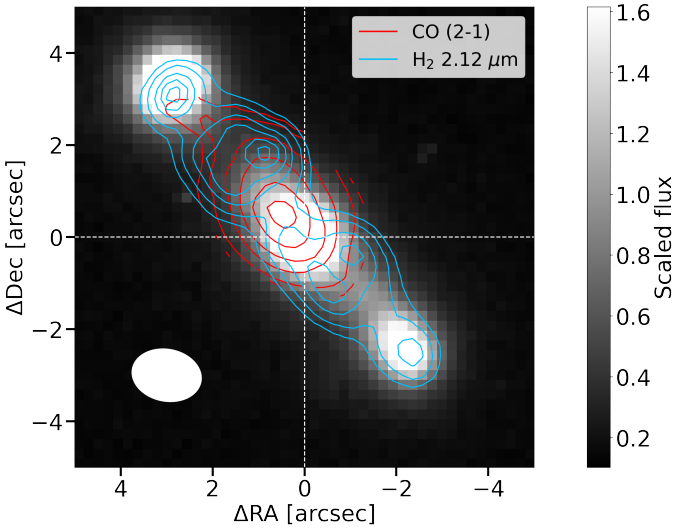

Fig. 9: Hα image of K4-47 with contours of H_2 from Akras et al. (2017) and CO (2–1) in blue and red, respectively. Contour levels are 10, 20, 40, 60, 80, and 95% of the peak flux of the corresponding images. The SMA beam is shown in white in the lower right. The H_2 contours have been shifted by –1″ in declination to account for misalignment in the astrometric solution of SMA and Gemini (see text). The dashed white cross indicates the centre of the Hα image, and the white ellipse indicates the synthesised beam size of the CO (2–1) SMA observations.

We measured the spectral index of K4-47 in the radio using the 1983 VLA data as well as VLA-NVSS data from 1994 (< 2.5 mJy; Condon & Kaplan 1998), Arcminute Microkelvin Imager survey observations (13.7 ± 2.7 mJy; Perrott et al. 2015), and VLASS observations from 2019 (3.69 ± 0.23 mJy; Gordon et al. 2021). The linear fit is parametrised by a slope of α 1.03±0.11 and an intercept of 0.73±0.54 (Fig. 10). Therefore, the fitted spectral index is $\alpha \approx 1.0$, which is consistent with thermal free-free emission in a medium with a fairly large density

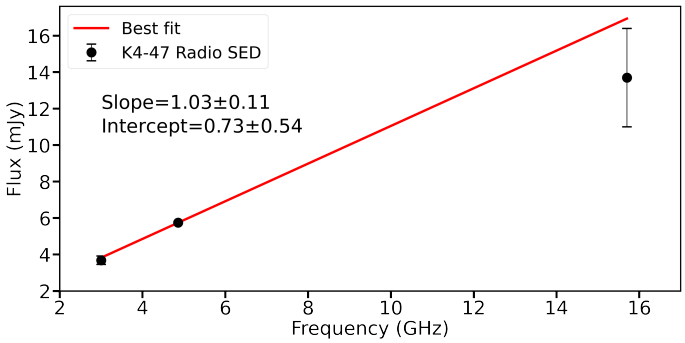

Fig. 10: Radio SED of K4-47 featuring our 5 GHz flux from the 1983 observations as well as the 3 GHz flux of Gordon et al. (2021) and the 15.7 GHz flux of Perrott et al. (2015).

gradient. This does assume no significant change in the source flux between measurements.

3.5. SED fitting

Given the apparent presence of circumstellar dust in the core of K4-47 (see Sect. 3.2), the dust temperature is key to derive the dust mass within the core of K4-47. This may also help better constrain the distance to the source, and give insight into the progenitor mass. We therefore attempted to derive the dust temperature from modified grey-body fitting to the spectral energy distribution (SED) of K4-47.

Using the NASA/IPAC Extragalactic database, we extracted the available photometry for K4-47 in the IR, which was obtained via the 2MASS and WISE surveys, as well as mid-IR photometry from the IRAS satellite. We also obtained optical photometry from the IGAPS survey catalogue for IPHAS, and included our SMA continuum flux, as well as the radio fluxes from the VLA and the literature (see Sect. 3.4). Fluxes were dereddened using our measured value for the core of E(B-V)=1.28, assuming R_ν=3.1 and using the extinction model of Fitzpatrick & Massa (2007). We then attempted to fit modified blackbodies of a certain temperature to the observed SED using in-house routines. The modified blackbodies were parametrised using the equation for dust mass (Hildebrand 1983):

$$M_d = \frac{F_\nu D^2}{\kappa_\nu B_\nu(T_d)}, \quad (3)$$

where F_ν is the flux at frequency ν, D is the distance to the source, κ_ν is the opacity in cm^2 g^{-1}, and $B_\nu(T_d)$ is the Planck function at an assumed dust temperature T_d. Rearranging for F_ν and defining $\kappa_\nu = \kappa_0 \left(\frac{\nu}{\nu_0}\right)$, we obtained the equation for the model flux:

$$F_\nu = A\, \kappa_0 \left(\frac{\nu}{\nu_0}\right)^\beta B_\nu(T_d), \quad (4)$$

where $A=M_d/D^2$. As K4-47 is heavily carbon-rich, we assume the dust is dominated by amorphous carbon grains following the dust opacity models of Preibisch et al. (1993), giving κ_0 = 0.65 cm^2 g^{-1} at frequency ν_0 =246.46 GHz.

We did not include our radio data in the fitting procedure, as the radio spectral index is consistent with thermal free-free emission (see Sect. 3.4). Initial fitting showed that the mid-IR–millimetre SED, covered by IRAS and SMA, is best replicated by a two-component modified blackbody. However, this did not

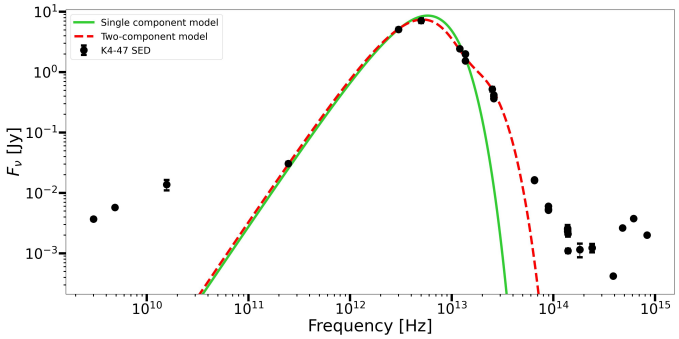

Fig. 11: K4-47 SED (black) overlaid with the best-fitting single (green) and double (red) component dust models.

fit the NIR-optical part of the SED. We attempted to fit the NIR-optical SED with a third hot dust component as well as a standard blackbody to resemble the central source. Neither method provided a reasonable fit to the NIR-optical SED. The results of both of these methods are shown in Appendix F. We found a good fit with both a single dust temperature and double-component model, when only the mid-IR and SMA fluxes were fitted, as shown in Fig. 11. When including the NIR 2MASS and WISE fluxes, IRAS fluxes were not well-fitted. This likely indicates that the NIR and optical fluxes are not dominated by dust, and have stellar or emission line or scattered light contributions that cannot be reproduced by our simplified dust models.

Figure 11 shows that the mid-IR and SMA fluxes are well resembled by a single dust temperature of 82 K. The fitted value of $\log_{10}(A)$=–11.57. This is equivalent to a dust mass range of 1.18×10^{-2}–0.89 $M_\odot$ across a distance range of 3–26.5 kpc. Assuming a gas/dust ratio of 100, this gives a total released mass range of 1.18–8.9 $M_\odot$ for the full distance range. Next, we compare our measured dust masses with the predicted initial and final masses to constrain the properties of the progenitor to K4-47, and also constrain the distance.

3.6. Progenitor, remnant, and nebula masses

We show the elemental abundance ratios of Gonçalves et al. (2004) and Henry et al. (2010) in Table 2. We also consider the isotopic ratios of Schmidt et al. (2018). We then compare these ratios to theoretical predictions of the chemistry surrounding post-AGB stars (Karakas & Lugaro 2016) at solar metallicity. The $^{12}C/^{13}C$=2.2 value implies a lower limit to the progenitor mass of 4 $M_\odot$, as at this initial mass the $^{12}C/^{13}C$ ratio drops significantly for the solar and sub-solar metallicity models. The large N/O ratios of Gonçalves et al. (2004) and Henry et al. (2010) (see Table 2), (N/O $\gtrsim$ 2.5 within errors), imply an initial mass of ~6 $M_\odot$, as at initial masses of 6 $M_\odot$, the N/O ratio drops back below 2.5 for the solar metallicity models of Karakas & Lugaro (2016). Therefore, we consider a progenitor mass of 4–6 $M_\odot$ for K4-47.

Recent studies of the WD initial-final mass relation (IFMR; Cummings et al. 2018; Marigo 2022) indicate that the resulting WD from 4–6 $M_\odot$ progenitor AGB stars range between 0.9–1.1 $M_\odot$, implying a total mass loss of 3.1–4.9 $M_\odot$. To compare, we calculate the total gas mass assuming a gas/dust ratio of 100, meaning the total gas mass is $101M_d$, where M_d is calculated using equation 3. The total gas mass exceeds the implied mass loss from the IFMR at 6 kpc, as the calculated total gas mass at 6 kpc is 5.78 $M_\odot$. We therefore suggest that the distance to K4-47 cannot exceed 6 kpc. This distance should be considered as an upper limit, as it is expected that some of the mass lost during the AGB phase would be contained within faint, extended halos (Villaver et al. 2002). Therefore, we would expect the detected mass of the nebula to be below the expected difference between the progenitor mass and the mass of the WD.

A distance upper limit of 6 kpc implies a separation between the core and the northern lobe of 0.13 pc. The outflow velocity at a distance of 6 kpc is 388±137 km s^{-1}, or a conservative upper limit of the velocity of ~500 km s^{-1}. If shocks do contribute to the excitation of the core emission, we would expect the shocks to decelerate the outflow. Therefore, the presence of shocks also implies an upper limit on the velocity. The mass upper limits are 4.7×10^{-2} $M_\odot$ for dust, and 2.77×10^{-3} $M_\odot$ for ionised gas, which gives a total detected nebula mass upper limit of 4.74 $M_\odot$for the nebula, assuming a gas/dust ratio of 100. The age of the nebula (336±119 yr) may be considered an upper limit, as the presence of shocks in the core may lead to deceleration of the outflows.

4. Discussion

4.1. The central source

Our SMA continuum and VLA 5 GHz observations indicate either a single stellar source or an unresolved compact binary within the core of K4-47. No symbiotic or binary properties have yet been discovered in K4-47, making any distinction between a single or binary central system difficult. The derived Zanstra effective temperature of 81 kK is consistent with a WD. In appendix G, we present GALEX survey images of the field of K4-47, showing a non-detection in the near-ultraviolet (λ_{rest}=2267 Å) band. The non-detection can be explained by the significant dust extinction we measure for the core. In Sect. 3.5 we show that the progenitor mass can be constrained to ~4–6 $M_\odot$, and that the corresponding expected final WD mass is 0.9–1.1 $M_\odot$. This assumes that the progenitor underwent the final thermal pulse stage.

The collimated outflow in K4-47 could originate from material accreting onto and being ejected by a companion to the central WD (such as for CK Vul, see Kamiński et al. 2021). This would mean the central system of K4-47 could potentially be a symbiotic star, which features mass transfer between a cool evolved star and a WD. However, the IR classification scheme developed for symbiotic stars (Akras et al. 2019b) show that PNe and post-AGB stars are distinct from symbiotic stars. Likewise, the IR colours for K4-47, $W1$–$W4$=10.33, K_s–$W3$=9.39, and J–H=0.79 mag, satisfy two of the three IR colour classification diagnostics for PNe (Akras et al. 2019a). The high W1-W4 and K-W3 colour indices are indicative a dusty source, and the IR colours therefore imply the absence of a symbiotic central system. However, we cannot rule out a companion in the centre that is not directly interacting with the WD.

Observed molecules also present some hints on the nature of the central object. HCO^+ (including isotopologues) is formed via dissociation of CO and H_2O and subsequent recombination. This can occur via two primary avenues. The first is via UV photodissociation (Kimura et al. 2012; Cleeves et al. 2017), and the second via collisional dissociation via shocks (Sánchez Contreras et al. 1997, 2000, 2015; Pulliam et al. 2011). The photodissociation route is associated with compact HCO^+ emission, as seen from the $H^{13}CO^+$ spatial distribution (Fig. C.1). This is consistent with a hot central source. The lack of $H^{13}CO^+$ emission in the lobes is inconsistent with the shock-dominated scenario presented by Gonçalves et al. (2004).

Our discussion of the central source of K4-47 is based mainly on our estimation of the Zanstra temperature of ~80 kK. However, the Zanstra method assumes only photoionisation excites the nebular gas. Comparing the position of the core of K4-47 in the diagnostic diagrams of Mari et al. (2023), in particular that of [O III] 4363/5007 versus [N II] 5755/6584 diagnostic ratio, we see that our measured ratios exceed the predicted ratios for photoionisation, implying an additional excitation mechanism. Likewise, we also compare our [S II]6716+6731, [N II]λ6583, and [O III]λ5007 line diagnostics with the models of Raga et al. (2008), adjusted from Fig. 6 of Gonçalves et al. (2009), in Fig. 12. We find that the core of K4-47 has similar diagnostic properties to the central core of PN He 1-1 (Gonçalves et al. 2009). The lobes are consistent with the high-velocity shock models of Raga et al. (2008). The strong [N I]λ5200 line (Table A.1) and high T_e found at the lobes are also indicative of fast shocks, in agreement with Gonçalves et al. (2004).

To test whether photoionisation dominates the excitation of the atomic gas in the core of K4-47, we examined the photoionisation models in the Mexican Million Models Database (3MdB; Morisset et al. 2015). We applied filters to examine models that were constructed using input blackbody files with temperatures between 70–90 kK, as well as models with predicted line ratios of [O III]4959+5007/Hβ, [N II]6548+6584/Hα, and [S II]6716+6731/Hα within 0.1 dex of the observed line ratios (Table A.1). A total of 18 models matched these constraints. We then filtered the remaining models based on the predicted ratios of He II, [N I]λ5198, [O I]λ6300, and [O III]λ4363 relative to Hβ. None of the remaining models predict line ratios within 0.1 dex of our observed ratios, although two models predicted [O I]λ6300/Hβ within 0.2 dex. In particular, the [O III]λ4363 line is underpredicted in 3MdB by ~2–3 orders of magnitude. It is therefore apparent that several of our line ratios cannot be explained by photoionisation only, and at least one additional excitation mechanism is required. Shock excitation is one such mechanism, which is supported by the unusually high T_e of 20 kK. To rule out photoionisation from a central source hotter than 90 kK, we conduct the same test using an upper blackbody temperature of 150 kK. We find that 3MdB still significantly underpredicts the line ratios of [N I]λ5198 and [O III]λ4363, meaning that shocks are still necessary to explain the observed line ratios.

An alternative cause of the high T_e is the low metallicity in the core of K4-47 (Table 2). The [N II]6584/5755 ratio is ~15, 26 and 24 for the core, northern lobe, and southern lobe, respectively. A lower ratio implies a higher T_e in the core than the lobes, despite the lobes being shock-dominated (Gonçalves et al. 2004). Therefore, shocks alone may not explain the high value of T_e measured for the core of K4-47. However, the range of models explored in 3MdB include those with sub-solar abundances, and lower than those determined for K4-47. These models include those that have input blackbody temperatures of 70–90 K. If the core was dominated by photoionisation, and the high T_e was due to the lower metallicity in K4-47, we would expect such models to be somewhat consistent with the line ratios we use to filter the 3MdB models. However, this is not the case. Therefore, whilst the lower metallicity may contribute to the high T_e, we still find that an additional heating mechanism such as shocks is required to explain the line ratios in K4-47.

The presence of shocks may have implications for the distance to K4-47. Our measured Zanstra temperature for the central WD of 80 kK is too low for a massive (~1 $M_\odot$) central star of a PN, even at such a young age. Such stars rapidly cross the Hertzprung-Russell (HR) diagram, reaching effective temperatures in excess of 200kK on timescales of just a few hundred years (Bloecker 1995; Miller Bertolami 2016). As such, the much lower Zanstra temperature could be an indication that the central WD is less massive than expected based on the nebular chemistry or that in this case the Zanstra temperature is unreliable due to either shocks or, perhaps more likely, the nebula not being optically thick. On the other hand, if the Zanstra temperature is accurate, this would require a significantly lower central star mass in order to be consistent with the kinematical age of the nebula, which in turn would imply a closer distance (otherwise the previously inferred nebular mass would exceed the AGB envelope mass, although this is heavily dependent on the assumed dust-to-gas ratio).

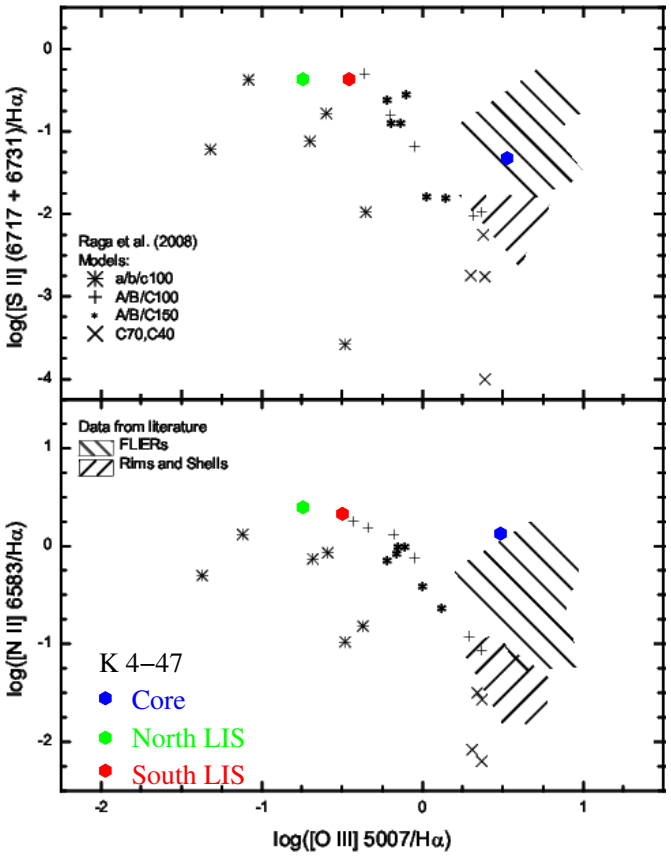

Fig. 12: Diagnostic diagrams of [S II]6717+6730 (top) and [N II]λ6583 (bottom) vs [O III]λ5007, as shown in Gonçalves et al. (2009). Black markers denote shock models from Raga et al. (2008), and diagonal lines indicate regions occupied by rims/shells and FLIERs. The numbers in the model names refer to the shock velocity of the models. Blue, green, and red markers show the position of the core, northern lobe, and southern lobe of K4-47, based on the measured emission line fluxes from the ALFOSC spectrum shown in Table A.1.

4.2. The circumstellar environment

The circumstellar environment that makes up the nebula of K4-47 consists of both atomic and molecular material. We see an elongated structure in CO and $H^{13}CN$ that is consistent with the bipolar structure of the Hα emission (Fig. 2). The sub-millimetre core emission traced by CO (2–1) and $H^{13}CN$ (3–2) shows a clear velocity gradient, as in Fig. 6. CO (2–1) shows a PA of 41°, but the $H^{13}CN$ emission has a PA of 13°. It is not clear if this discrepancy in the PA of different molecular lines is a

signature of multi-polar outflows, as seen in other PNe (Akras & Gonçalves 2016; García-Segura et al. 2021; Gómez-Muñoz et al. 2023; Wen et al. 2024), or a consequence of the smaller source size of K4-47 in $H^{13}CN$ compared to CO, which means that the emission is less spatially resolved. It is also possible that the much higher optical depth of CO makes direct comparison to HCN inadequate, as it shows only the outer layer of CO gas.

To test if the PA of the molecular and atomic gas phase match, we examined the flux density of the jets in the CO PV diagrams extracted at different PAs. We found that the flux density peaked at a PA of 41°± 1°, indicating that the CO gas matches the PA of the atomic gas (Gonçalves et al. 2004).

Our analysis of the expansion of the optical lobes shows an approximate optical outflow velocity of ∼few hundreds km s^{-1}. This is an order of magnitude greater than the CO outflow velocity (∼50–60 km s^{-1}). Previous optical studies of K4-47 (Corradi et al. 2000; Gonçalves et al. 2004) have indicated that the lobe emission is powered by shocks. We also see that the tip of the northern CO outflow meets the northern lobe seen in optical and H_2 emission. This could be explained by molecular material that has been shaped by the atomic outflow, although this would not explain the narrow widths of the molecular lines. The presence of H_2 gas tracing the cavities of the bipolar atomic outflow (Akras et al. 2017) suggests that the molecular environment formed first, with the atomic outflow triggering at a later time and 'punching' through the molecular material, simultaneously shaping the molecular environment and interacting with the molecular material via shocks that produce the H_2 emission. The atomic outflow then terminates at the lobes.

In Sect. 3.2, we show that the core has significant circumstellar dust extinction of 0.3–0.6 mag from $\sim 10^{-2}$ $M_\odot$ of dust. The dust mass is about 1 order of magnitude higher than measurements of other PNe (Koller & Kimeswenger 2001; Clayton et al. 2013; Van de Steene et al. 2015; Lau et al. 2016; Otsuka et al. 2017; Toalá et al. 2021). The relatively high dust mass is beyond the upper limit derived in the models of Ventura et al. (2025), and is consistent with the theoretical range of dust surrounding post-AGB stars (10^{-4}–10^{-2} $M_\odot$; Ferrarotti & Gail 2006; Zhukovska & Henning 2013; Ventura et al. 2014, 2020). Therefore, the dust may have formed during the post-AGB phase in conjunction with the compact molecular CSM, before the bipolar outflows were triggered and the source reached the PN phase.

4.3. Comparison to CK Vul

CK Vul is a Galactic luminous red nova (LRN) produced by a WD-red giant merger (Kato 2003; Kamiński et al. 2015) that resulted in a 1670 eruption (Shara & Moffat 1982). In the past few years, it has been extensively observed and characterised in a wide range of wavelengths (e.g. Hajduk et al. 2007; Evans et al. 2016; Tylenda et al. 2019; Kamiński et al. 2021; Tylenda et al. 2024). The source shows a clear bipolar structure in Hα that spans 71″ (Hajduk et al. 2007, 2013), as well as a clumpy core that surrounds the merger remnant. As mentioned, it bears many observational similarities to K4-47, which we critically review below.

Both sources exhibit a bipolar structure, primarily in atomic emission. The tips of the lobes at the most extended regions of CK Vul are shock-excited (Banerjee et al. 2020), and show molecular emission towards the central region (Kamiński et al. 2017, 2018, 2020). The age of both sources is similar: our age estimate of K4-47 336±119 yr is almost exactly 355 yr that past since the 1670 eruption of CK Vul.

In both objects, we see a compact (∼0.″1) radio source at 5 GHz (see Fig. 8 for K4-47, for CK Vul see Hajduk et al. 2007) that is close to the centre of symmetry in the bipolar structure, but not overlapping with the optical knots. The 5 GHz flux of K4-47 (5.75 mJy, see Sect. 3.4), is a factor of ∼4 larger than for CK Vul (1.5 mJy Hajduk et al. 2007). Hajduk et al. (2007) suggested that the radio emission of CK Vul originated from thermal free-free emission in an optically thick medium. The measured spectral index for K4-47 of $\alpha_\nu \approx 1$ (see Sect. 3.4) indicates the radio emission is consistent with thermal free-free emission in a optically thick medium, but due to the opacity, we cannot rule out shock-induced radio emission, as has been suggested for CK Vul by Kamiński et al. (2020).

Across the various sub-millimetre/millimetre studies of K4-47, a plethora of molecules have been detected (see Sect. 3.3), many of which are seen in CK Vul. CO, CN, SiO, HCO^+, HCN, HNC, CS, CH_3CN, CCH, H_2CO, and N_2H^+ (including isotopologues of ^{13}C and ^{15}N) have all been detected in CK Vul. The molecular environments extend out to 3.″41 for K4-47 and 6.″7 for CK Vul (Kamiński et al. 2020). Assuming distances of 5.9 kpc (Tajitsu & Tamura 1998) and 3.5 kpc (Kamiński et al. 2021), and inclination angles (i) of 67.5° (Corradi et al. 2000) and 25° (Kamiński et al. 2021) for K4-47 and CK Vul, respectively, we calculate the deprojected extent of the most extended molecular emission to be 0.10 pc for K4-47 and 0.12 pc for CK Vul. The similar extent for the molecular environments in both sources, along with the similar nebula ages, indicates that the molecular CSEs of K4-47 and CK Vul may have been produced or evolved (i.e. shaped by bipolar outflows) via the same mechanism and on similar timescales. For the extended optical emission, we get deprojected distances of 0.17 pc for K4-47 and 2.87 pc for CK Vul, based on the northern lobe for K4-47 and using the upper limit of i=15° for the Hα hourglass structure in CK Vul (Kamiński et al. 2021).

Isotopic abundances of ^{13}C, ^{15}N, and ^{17}O were found to be enriched in K4-47 by Schmidt et al. (2018), similar to CK Vul. This led to the idea that both sources have similar origins. In Fig. 1, we plot the calculated $^{12}C/^{13}C$ vs $^{14}N/^{15}N$ isotopic ratios for K4-47 (Schmidt et al. 2018) and CK Vul (Kamiński et al. 2017), as well as CRL 618 (Wannier et al. 1991), Orion KL (Wannier et al. 1991). IRAS 19312+1950 (Qiu et al. 2023). CRL 618 and CRL 2688 are carbon-rich pre-PNe that also show isotopic enrichment in ^{13}C and ^{15}N (Wannier et al. 1991). IRAS 19312+1950 is an embedded star within a giant molecular cloud that shows characteristics of both a young stellar object (Cordiner et al. 2016) and an evolved star (Nakashima et al. 2015), and has also been proposed as a candidate stellar merger remnant (Qiu et al. 2023). Also plotted are the ratios for SiC presolar grains from the Presolar Grains Database (PGD; Stephan et al. 2024). The grains featured include mainstream, X, Y, and Z grains. Mainstream grains are representative of the most commonly detected SiC grains in the Milky Way, and may partly originate from low-mass, C-rich AGB stars with solar metallicity, although they show a wide range of C, O, and Si abundances (see Stephan et al. 2024, and references within). Y and Z grains are believed to have similar origins from mainstream grains, but with lower metallicities, whilst X grains are believed to originate from core-collapse supernovae (ccSNe; Hoppe et al. 1996, 2000). The isotopic ratios of both K4-47 and CK Vul are consistent with 'nova' grains, and the carbon isotopic ratios are also consistent with A+B grains, which are connected with J-type stars (Liu et al. 2017). To compare the predicted and observed isotopic ratios of J-type carbon stars, we also include the observed isotopic ratios of VX And and Y Cvn, both of which are

classified as J-type carbon stars (Abia et al. 2017). Interestingly, the origin of J-type stars has been attributed to a He-WD + RGB mergers (Liu et al. 2017), the same progenitor system suggested for CK Vul (Tylenda et al. 2024). Therefore, we reiterate the postulate that the progenitor of K4-47 may have been a J-type carbon star, which can explain the exotic carbon chemistry of the molecular environment (Schmidt & Ziurys 2019).

In Table 2, we show the elemental abundances of K4-47 (Gonçalves et al. 2004; Henry et al. 2010) and CK Vul (Tylenda et al. 2019). The K4-47 abundances of Gonçalves et al. (2004) and Henry et al. (2010)[7] are broadly consistent within percentage errors. The ratios of He/H and O/H are a factor of roughly two to three less in K4-47 compared to CK Vul, S/H is about three to four times less, and Ne/H is a factor of seven less. Only the N/O ratio is larger in K4-47, by a factor of two. The nitrogen abundances (N/H, N/O) are enhanced by more than an order of magnitude compared to solar values (Asplund et al. 2009), whilst abundances of O, Ne, and S are all lower than the solar values for both K4-47 and CK Vul.

CK Vul is known as a nitrogen-rich source, based on submillimetre studies (Kamiński et al. 2015; Kamiński et al. 2017), and made clear by the elemental abundances shown in Table 2. K4-47 exhibits an even higher N/O ratio, implying that H-burning in CNO cycles has processed material into nitrogen (see discussion of Tylenda et al. 2019). We therefore classify K4-47 as a nitrogen-rich source. The apparent enhancement of nitrogen-bearing species in envelopes of evolved stars could also come from shock chemistry without the need for CNO processing, as was found for the evolved source OH231.8+4.2 (Sánchez Contreras et al. 2015).

Despite the similarities outlined above, we see many differences as well. The isotopic abundances of ^{18}O are noticeable, with no ^{18}O-bearing molecules detected in K4-47, unlike CK Vul where it is highly enhanced (^{16}O/^{18}O≈36; Kamiński et al. 2017). The identification of raised ^{18}O for CK Vul was a key characteristic that led to the hypothesis that partial carbon burning is responsible for some of the isotopic ratios in CK Vul. Another key difference between K4-47 and CK Vul is the lack of detection of ^{26}Al in K4-47, which was detected in the form of ^{26}AlF in CK Vul (Kamiński et al. 2018). All these isotopic differences may indicate that both objects went through different nucleosynthesis paths, but by themselves do not exclude a merger scenario for K4-47, as the chemistry of merger remnants is still not well understood.

We also highlight differences in our optical spectrum of K4-47 compared to CK Vul (Fig. 14). CK Vul is missing some prominent lines seen in K4-47, namely [O III]λ4363, HeII λ4685, NII λ4643, and [Ar V]λ7006. The [N II]$\lambda\lambda$6548,6583 and [S II]$\lambda\lambda$6716,6731 doublets are both much stronger in CK Vul than K4-47 (relative to Hβ), as is Hα. The derived physical properties of the atomic gas are also different, with the value n_e derived for CK Vul (Tylenda et al. 2019) differing somewhat from our values derived for K4-47. Tylenda et al. (2019) derive values of $130 < n_e < 600$ cm^{-3} for different kinematic components, an order of magnitude less than for K4-47. This implies a much denser environment for K4-47, despite the similar ages, and thus also a higher total ejecta mass for K4-47 as well as a higher overall mass-loss rate.

We did not detect an extended optical nebula, as that seen in Hα emission for CK Vul (Hajduk et al. 2007). In Fig. 13, we compare the two sources in Hα at the same deprojected spatial scale. Here, we assume distances of 5.9 kpc for K4-47 (Tajitsu & Tamura 1998) and 3.5 kpc for CK Vul (Kamiński et al. 2021). We can see that the optical lobes of K4-47 barely extend beyond the central clumpy region of CK Vul, although the extent of the molecular environments of both sources are comparable. No extended Hα structure is seen in K4-47, and assuming that the extent of any such extended structure was present, it would have been covered in the ALFOSC FoV. However, the H_2 emission shown in Fig. 9 traces the cavity walls of the optical outflow as it propagates through the circumstellar medium (Akras et al. 2017), which indicates the presence of an extended circumstellar component that is not detected in our observations. This is supported by the fact that the lobes are shock-dominated (Gonçalves et al. 2004). The mass-loss mechanism for the undetected circumstellar gas is unclear, but may be due to an AGB wind, binary interactions, or even merger ejecta. It is not clear if any extended structure in K4-47 would resemble, morphologically or kinematically, the extended Hα structure surrounding CK Vul. We also observe that the dust mass in K4-47 (~few 10^{-2} $M_\odot$) is an order of magnitude larger than for CK Vul (Banerjee et al. 2020).

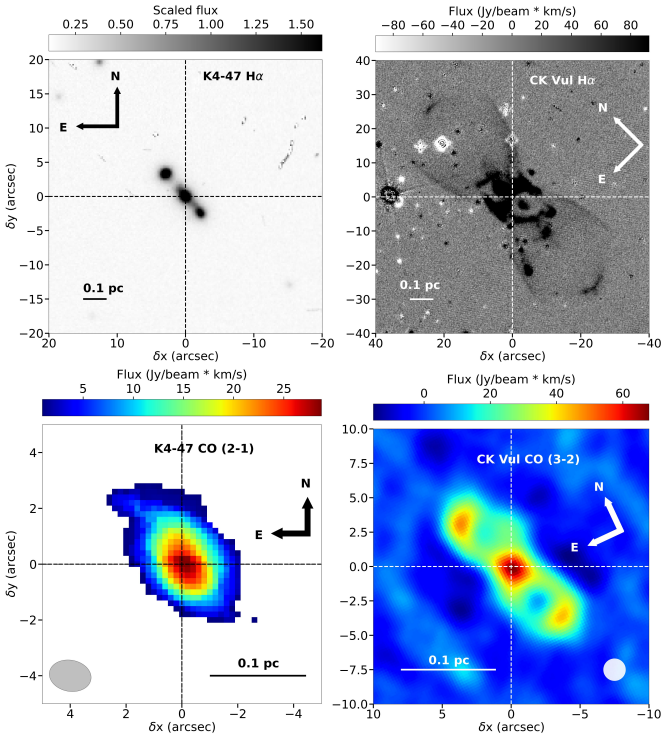

Fig. 13: K4-47 (left column) and CK Vul (right column) compared at the same equivalent spatial scale. The top row compares the Hα distribution with the image of CK Vul taken from Hajduk et al. (2007). The bottom row compares the CO distribution with the CO (2–1) for K4-47 from our SMA data and the CO (3–2) for CK Vul from Kamiński et al. (2020). The images of CK Vul were rotated to match the orientation of K4-47.

The kinematics of the CSM for both sources are also considerably different. Although for both sources we see a fast atomic outflow/expansion velocity, with a much slower (by ~1 order of magnitude compared to the atomic outflow) molecular outflow, the measured velocities are very different. Whilst the expansion velocity of the shocked tips in CK Vul is of the order of ~1700 km s^{-1}, the atomic outflow in K4-47 is much slower, at 350

[7] For Henry et al. (2010), abundances of K4-47 were extracted from the online data repository on Vizier: https://vizier.cds.unistra.fr/viz-bin/VizieR-3?-source=J/ApJ/724/748/table5

Table 2: Elemental number abundances of K4-47 and CK Vul. Percentage errors are shown in parentheses.

Element	K4-47[1]		CK Vul[2]	Solar[3]
	Gonçalves+	Henry+		
He/H	0.139 (14%)	0.09 (13%)	0.260 (21%)	0.085
N/H	3.74×10^{-4} (40%)	1.4×10^{-4} (22%)	1.69×10^{-4} (29%)	6.76×10^{-5}
O/H	7.37×10^{-5} (32%)	4.9×10^{-5} (15%)	1.22×10^{-4} (34%)	4.90×10^{-4}
Ne/H	1.74×10^{-5} (66%)	1.00×10^{-5} (22%)	7.45×10^{-5} (29%)	8.50×10^{-5}
S/H	1.96×10^{-6} (48%)	1.50×10^{-6} (23%)	5.70×10^{-6} (9%)	1.32×10^{-5}
N/O	5.07 (51%)	2.90 (20%)	1.39 (45%)	0.14

Notes. [1]K4-47 elemental abundances are taken from Gonçalves et al. (2004) and Henry et al. (2010).
[2]CK Vul abundances are taken from Tylenda et al. (2019).
[3]Solar values are taken from Asplund et al. (2009).

km s^{-1}. As seen in Table 3, the atomic outflow in K4-47 and the molecular outflow in CK Vul show similar velocities, which may explain why the optical nebula and molecular environment in K4-47 and CK Vul, respectively, extend across similar spatial scales (see Fig. 13).

There is no consensus on the central source of CK Vul. Previous studies have assumed a central WD, supported by the proposed mechanism of thermal free-free emission to power the 5 GHz radio emission (Hajduk et al. 2007), and the presence of the [O IV]λ25.89 μm line (Evans et al. 2016). However, Kamiński et al. (2021) calculated the molecular lifetimes for the lobes in CK Vul when exposed to different levels of radiation shielding by dust. The only combination of stellar radiation and dust shielding that produces molecular lifetimes greater than the nebula age of CK Vul (and so explaining the rich molecular content) is a central WD with $T_{\rm eff}\approx$20 kK with extinction between the WD and the lobes of $A_V>>3$ mag. This, however, is improbable as such a WD gives a luminosity of ~0.1 $L_\odot$, inconsistent with the derived source luminosity of ~1 $L_\odot$ (Kamiński et al. 2015). Likewise, the extinction value along the lobe-central star axis is unlikely to be as high as A_V=3 mag (Tylenda et al. 2019). Kamiński et al. (2021) also re-identified the [O IV]λ25.89 μm line as the [Fe II] a^6 D 7/2→9/2 line, which does not require a hot central source. Kamiński et al. (2021) subsequently argue that the central star of CK Vul may have the characteristics of a cool, evolved star, similar to other Galactic red novae (Tylenda 2005; Tylenda et al. 2011). Kamiński et al. (2021) also argue that the remnant circumstellar structure can be explained by a binary system, making the progenitor of CK Vul a triple system. This can also explain the launching of jets in PNe, and so may be applicable to K4-47.

Contrary to the case of CK Vul, our results indicate that the central source of K4-47 is almost certainly a WD. This is the main reasoning behind excluding the stellar merger scenario for K4-47 because if CK Vul does host a cool evolved merger remnant (as observed for other Galactic LRNe), it would be a key identifying feature for classifying LRNe at later times, even for stellar mergers involving a WD.

The phenomenological comparison of both sources we have presented here cannot be fully conclusive, but we favour the scenario that K4-47 maybe a genuine, albeit very young, planetary nebula. As postulated by Schmidt et al. (2018), the progenitor of the system may be a J-type AGB star, which created the molecular circumstellar environment rich in molecules that are traced at millimetre wavelengths. Dust may have also formed at this time. This cool molecular cocoon was later punched by a pair of slightly asymmetric jets, which we now observe mainly in atomic and H_2 emission. Some of the circumstellar wind was swept out by the jets, which is manifested by the CO extensions observed at high velocities and largest distances from the centre. Just as in CK Vul, the jets may be created by a companion to the component that was the source of the circumstellar material.

4.4. Analogy to other evolved sources

As well as PNe and CK Vul, K4-47 bears some resemblance to a subset of evolved stellar systems known as water fountains (WFs; Imai 2007; Desmurs 2012). WFs are often characterised by collimated bipolar jets and high-velocity ($\gtrsim$ 100 km s^{-1}) H_2O masers. Other components seen are low-velocity ($\lesssim$ 20–40 km s^{-1}) central toroidal components (Gómez et al. 2008), and strong optical extinction (Suárez et al. 2008; Gómez et al. 2015).

On initial inspection, K4-47 possesses multiple morphological similarities with WFs. These include collimated bipolar outflows with velocities exceeding 100 km s^{-1}, a molecular gas phase, strong apparent obscuration in the optical, as inferred by the GALEX non-detection (Fig. G), and the lack of stellar features from the central WD. Khouri et al. (2022) also found that some WFs have high isotopic enrichment of ^{17}O and ^{18}O, which implies initial masses of 1.8–4.0 $M_\odot$. Such stars are expected to become carbon stars eventually (Abia et al. 2017), including J-type carbon stars, which we propose as the likely progenitor of K4-47. However, WFs are partly defined by their oxygen-rich chemistry, indicating that the AGB evolution of WFs may have been interrupted. Khouri et al. (2022) attribute this to substantial mass loss on short timescales, which they attribute to CEE.

Despite the similarities, there are some glaring differences. Firstly, our progenitor mass estimate for K4-47 is not consistent with the masses of WF stars from Khouri et al. (2022). K4-47 is also dominated by carbon-bearing molecules, as opposed to WF sources, which feature oxygen-rich chemistry (Gómez et al. 2008, 2015, 2018). The fast outflows seen in WFs are seen typically in the molecular phase, whereas our molecular outflow is 56 km s^{-1}, which is a factor of ~2 slower than the molecular outflows typically seen in WFs.

Another issue is the dynamical age of the molecular outflow. Typically, WF jet ages span ~100–200 yr (Tafoya et al. 2019), an order of magnitude less than what we find for the molecular outflow in K4-47. Lastly, the molecular environment shows little to no evidence of a toroidal component (Figs. 7 and D.1), due to the extended elongated structure that traces the atomic outflow, and we see no velocity gradient in the PV diagram perpendicular to the outflow (see Fig. D.1). Such a structure would be expected to be expanding in a post-CEE source, as well as in LRNe (Nandez et al. 2014; Pejcha et al. 2017). However, we cannot conclude such a structure is not present in K4-47, due to the insufficient spatial resolution of our sub-millimetre observations, which can resolve the overall molecular structure but not the innermost re-

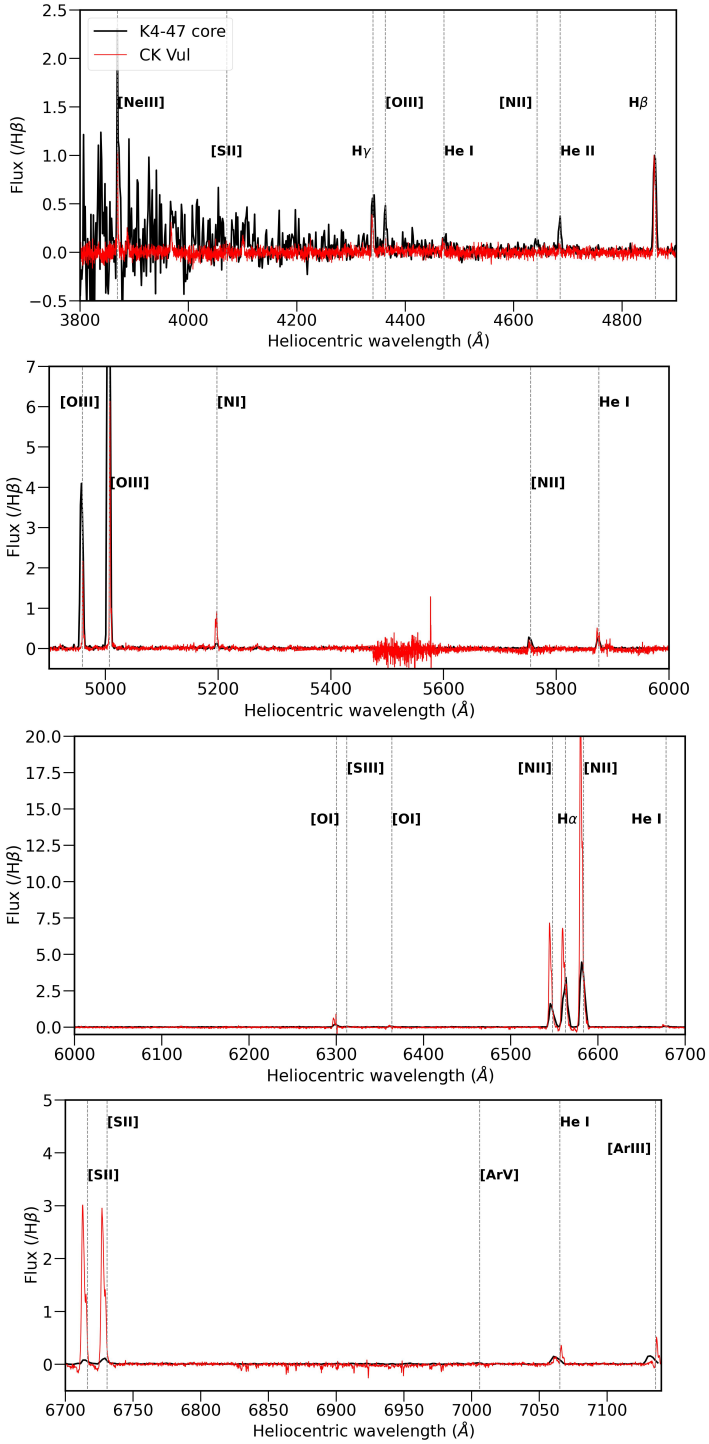

Fig. 14: ALFOSC K4-47 total spectrum across all three components compared to the Tylenda et al. (2019) VLT-XShooter spectrum of CK Vul. Both spectra have been normalised to Hβ. The y-axes have been truncated to show the weaker lines in more detail. The K4-47 spectrum is in the heliocentric rest frame, and the CK Vul spectrum has been shifted by –150 km s^{-1} to align the majority of lines from both spectra.

gion. We summarise the overall properties of K4-47, CK Vul, and WFs, in Table 3.

Although WFs are typically oxygen-rich sources, this could be a bias based on their characteristic feature: high-velocity water masers. Theoretically, carbon-rich progenitor stars can also undergo CEE and mass-loss. However, it is unclear exactly what a carbon-rich post-CEE system would look like. One such example is PN G054.2-03.4 (The Necklace; Viironen et al. 2009), which is believed to be a post-CE carbon-rich PN (Miszalski et al. 2012), but likely features an accretion disc - which K4-47 does not seem to have.

Both the similarities and differences between K4-47 and WFs highlight the difficulty in understanding stellar evolution, particularly post-CEE sources. It is clear that the evolution path for evolved stellar systems hosting carbon-rich stars is still not well understood, but some of the morphological similarities between K4-47 and WF sources might be a clue to understanding these systems. Despite this, the lack of a torus in K4-47 is indicative of no previous CEE phase. Therefore, the similar morphologies mean that the evolution of such sources needs to be investigated further to adequately understand how carbon-rich systems evolve beyond the CE phase, as well as how similar morphologies can be produced by objects of different origins and evolutionary phase.

5. Summary

In this paper, we have examined the atomic and molecular environment of the unusual PN K4-47 to investigate the similarities between the source and other stellar classifications and as an attempt to better understand the origins of the source. Our data include the first spatially resolved millimetre molecular maps of the source. Our findings are described below.

- The source is bipolar not only in optical emission and shocked H_2 but also in molecular emission. We observed a clear velocity gradient approximately along the atomic outflow PA, which implies a maximum molecular outflow velocity of 56 km s^{-1}.
- We determined the physical constraints on the circumstellar gas within the core. From forbidden [N II] and [S II] line ratios, we estimate the electron temperature to be 19900 ± 1200 K and the electron density to be 2800 ± 700 cm^{-3}.
- Using the Zanstra method and the He II λ4686/Hβ line ratio for the core, we estimated a stellar effective temperature T_{eff} = 81 ± 2 kK, implying a central WD.
- Using grey-body fitting to the SED of K4-47, we have shown that the dust-dominated region of the SED can be fitted by a dust temperature of 82 K. The isotopic and elemental abundances of K4-47 indicate an initial mass of 4–6 M$_\odot$, which implies a current WD mass of ~1 M$_\odot$. The dust and gas mass is consistent with the total released mass of 3–5 M$_\odot$at distances ≤ 6 kpc. The nebula mass is dominated by neutral atomic gas, with ~ a few 10^{-2} M$_\odot$of dust and ~ a few 10^{-3} M$_\odot$of ionised gas.
- The spatial change in the northern optical lobe moving away from the centre of symmetry along the bipolar PA implies an atomic outflow velocity of 350 ± 88 km s^{-1} at a distance upper limit of 6 kpc.
- By comparing our line ratios to 3MdB photoionisation models, we find that photoionisation alone cannot explain the excitation of the atomic gas. The high value of T_e supports this statement, although the low metallicity of K4-47 may contribute to the high measured T_e. However, low metallicity alone cannot explain the high value of T_e, and ultimately an additional heating mechanism is required, which we attribute to shocks originating from interaction between the bipolar outflows and the circumstellar environment in the core of K4-47.

Table 3: Qualitative comparison of various stellar sources and stellar classifications discussed in this work. Certain properties, for instance, the central source temperature of WFs, are not well constrained and therefore represent an approximate range.

Source	Central star T_{eff} (kK)	Age (yr)	Collimated jets	Extended nebula	Shocks	Isotopic enrichment	Expansion velocity (molecular/atomic, km s^{-1})
K4-47	81±2	400–900	✓	×	✓	✓	56/350
CK Vul	?	357	✓	✓	✓	✓	312/1700
LRNe	2–3	< 40	✓[1]	✓	✓	×[2]	~200 for both
WFs	3—30[3]	100–200	✓	Sometimes	✓	✓	100–200

Notes. [1]Except for OGLE-2002-BLG-360.
[2]Except for CK Vul.
[3]Heavily dependent on mass and evolutionary stage, uncertain.

- The lack of an extended nebula coupled with the clear presence of shocks and H_2 emission in the walls of the collimated outflows imply earlier mass loss long before the atomic outflow was triggered. This is supported by the dynamical age (≈1900 yr) of the molecular outflow. The dynamical age of the atomic outflow is 336 ± 119 yr. It is possible that the shocks that excite H_2 occur as the atomic outflow collides with the older molecular outflow.
- The old red nova CK Vul and K4-47 show some clear similarities in morphology, kinematics, and chemistry. However, the central source of K4-47 likely being a WD is inconsistent with other Galactic merger remnants, including CK Vul.

Overall, our results suggest that K4-47 can be classified as a PN, although the chemistry, WD age and mass, and nebula age indicate it is an unusual PN. To examine K4-47 further, we would first require separate, non-blended spectra of the three components in the optical to be able to investigate the lobes in more detail and address their exact nature and therefore better understand the mass-loss history of the source. Deeper sub-millimetre observations would also help in examining the spatial distribution of certain molecules, such as HCO^+, and higher-excitation lines, which can potentially trace shocks. High-resolution imaging of the core can help in investigating any possible sub-structures, including shocked regions, in the core. Finally, a dedicated search for a companion star in the central system using deeper radio observations with sufficient angular resolution would be useful.

This study also highlights the difficulty of identifying LRNe at late times, considering the many similarities that LRNe have with many other classifications of evolved stellar sources.

Acknowledgements. TS would like to thank R. Tylenda for his helpful discussions. TS and TK acknowledge funding from grant no 2018/30/E/ST9/00398 from the Polish National Science Center. DJ acknowledges support from the Agencia Estatal de Investigación del Ministerio de Ciencia, Innovación y Universidades (MCIU/AEI) under grant "Nebulosas planetarias como clave para comprender la evolución de estrellas binarias" and the European Regional Development Fund (ERDF) with reference PID2022-136653NA-I00 (DOI:10.13039/501100011033). DJ also acknowledges support from the Agencia Estatal de Investigación del Ministerio de Ciencia, Innovación y Universidades (MCIU/AEI) under grant "Revolucionando el conocimiento de la evolución de estrellas poco masivas" and the European Union NextGenerationEU/PRTR with reference CNS2023-143910 (DOI:10.13039/501100011033). DRG acknowledges the grants of the Brazilian agencies FAPERJ (E-26/200.467/2026) and CNPq (315307/2023-4). The Submillimeter Array is a joint project between the Smithsonian Astrophysical Observatory and the Academia Sinica Institute of Astronomy and Astrophysics and is funded by the Smithsonian Institution and the Academia Sinica. We recognise that Maunakea is a culturally important site for the indigenous Hawaiian people; we are privileged to study the cosmos from its summit. Based on observations made with the Nordic Optical Telescope, owned in collaboration by the University of Turku and Aarhus University, and operated jointly by Aarhus University, the University of Turku and the University of Oslo, representing Denmark, Finland and Norway, the University of Iceland and Stockholm University at the Observatorio del Roque de los Muchachos, La Palma, Spain, of the Instituto de Astrofisica de Canarias. The NOT data were obtained under program ID P70-404. The National Radio Astronomy Observatory is a facility of the U.S. National Science Foundation operated under cooperative agreement by Associated Universities, Inc.

References

Aaquist, O. B. & Kwok, S. 1990, A&AS, 84, 229
Abia, C., Hedrosa, R., Domínguez, I., & Straniero, O. 2017, A&A, 599, A39
Akras, S. & Gonçalves, D. R. 2016, MNRAS, 455, 930
Akras, S., Gonçalves, D. R., & Ramos-Larios, G. 2017, MNRAS, 465, 1289
Akras, S., Guzman-Ramirez, L., & Gonçalves, D. R. 2019a, MNRAS, 488, 3238
Akras, S., Leal-Ferreira, M. L., Guzman-Ramirez, L., & Ramos-Larios, G. 2019b, MNRAS, 483, 5077
Amôres, E. B., Jesus, R. M., Moitinho, A., et al. 2021, MNRAS, 508, 1788
Amôres, E. B. & Lépine, J. R. D. 2005, AJ, 130, 659
Asplund, M., Grevesse, N., Sauval, A. J., & Scott, P. 2009, ARA&A, 47, 481
Balick, B. & Frank, A. 2002, ARA&A, 40, 439
Banerjee, D., Geballe, T., Evans, A., et al. 2020, ApJ, 904, L23
Bloecker, T. 1995, A&A, 299, 755
Cahn, J. H., Kaler, J. B., & Stanghellini, L. 1992, A&AS, 94, 399
Cardelli, J. A., Clayton, G. C., & Mathis, J. S. 1989, AJ, 345, 245
Clayton, G. C., Bond, H. E., Long, L. A., et al. 2013, ApJ, 771, 130
Cleeves, L. I., Bergin, E. A., Öberg, K. I., et al. 2017, ApJ, 843, L3
Condon, J. & Kaplan, D. 1998, ApJSupplement Series, 117, 361
Cordiner, M., Boogert, A., Charnley, S., et al. 2016, ApJ, 828, 51
Corradi, R. L. M., Gonçalves, D. R., Villaver, E., et al. 2000, ApJ, 535, 823
Cummings, J. D., Kalirai, J. S., Tremblay, P.-E., Ramirez-Ruiz, E., & Choi, J. 2018, ApJ, 866, 21
Desmurs, J.-F. 2012, Proceedings of the IAU, 8, 217
Edwards, J. L., Cox, E. G., & Ziurys, L. M. 2014, ApJ, 791, 79
Endres, C. P., Schlemmer, S., Schilke, P., Stutzki, J., & Müller, H. S. 2016, JMS, 327, 95
Evans, A., Gehrz, R. D., Woodward, C. E., et al. 2016, MNRAS, 457, 2871
Ferrarotti, A. & Gail, H.-P. 2006, A&A, 447, 553
Fitzpatrick, E. & Massa, D. 2007, ApJ, 663, 320
Gaia Collaboration, Brown, A. G. A., Vallenari, A., et al. 2021, A&A, 649, A1
García-Segura, G., Taam, R. E., & Ricker, P. M. 2021, ApJ, 914, 111
Gómez, J. F., Niccolini, G., Suárez, O., et al. 2018, MNRAS, 480, 4991
Gómez, J. F., Suárez, O., Bendjoya, P., et al. 2015, ApJ, 799, 186
Gómez, J. F., Suárez, O., Gómez, Y., et al. 2008, AJ, 135, 2074
Gómez-Muñoz, M., Vázquez, R., Sabin, L., et al. 2023, A&A, 676, A101
Gonçalves, D., Mampaso, A., Corradi, R., & Quireza, C. 2009, MNRAS, 398, 2166
Gonçalves, D. R., Corradi, R. L. M., & Mampaso, A. 2001, ApJ, 547, 302
Gonçalves, D. R., Mampaso, A., Corradi, R. L. M., et al. 2004, MNRAS, 355, 37
Gordon, Y. A., Boyce, M. M., O'Dea, C. P., et al. 2021, ApJS, 255, 30
Green, G. M., Schlafly, E., Zucker, C., Speagle, J. S., & Finkbeiner, D. 2019, ApJ, 887, 93
Green, G. M., Schlafly, E. F., Finkbeiner, D., et al. 2018, MNRAS, 478, 651
Green, G. M., Schlafly, E. F., Finkbeiner, D. P., et al. 2015, ApJ, 810, 25
Hajduk, M., van Hoof, P. A. M., & Zijlstra, A. A. 2013, MNRAS, 432, 167
Hajduk, M., Zijlstra, A. A., van Hoof, P. A. M., et al. 2007, MNRAS, 378, 1298
Henry, R. B. C., Kwitter, K. B., Jaskot, A. E., et al. 2010, ApJ, 724, 748
Hildebrand, R. H. 1983, QJRAS, 24, 267
Hoppe, P., Strebel, R., Eberhardt, P., Amari, S., & Lewis, R. S. 1996, Science, 272, 1314
Hoppe, P., Strebel, R., Eberhardt, P., Amari, S., & Lewis, R. S. 2000, Meteoritics and Planetary Science, 35, 1157

Huggins, P. J., Bachiller, R., Planesas, P., Forveille, T., & Cox, P. 2005, ApJS, 160, 272
Imai, H. 2007, Proceedings of the IAU, 3, 279
Ivanova, N., Justham, S., Chen, X., et al. 2013, A&A Rev., 21, 59
Jones, D. & Boffin, H. M. J. 2017, Nature Astronomy, 1, 0117
Kaler, J. B. & Jacoby, G. H. 1991, AJ, 372, 215
Kamiński, T., Menten, K. M., Tylenda, R., et al. 2015, Nature, 520, 322
Kamiński, T., Menten, K. M., Tylenda, R., et al. 2017, A&A, 607, A78
Kamiński, T., Menten, K. M., Tylenda, R., et al. 2020, A&A, 644, A59
Kamiński, T., Schmidt, M., & Tylenda, R. 2010, A&A, 522, A75
Kamiński, T., Steffen, W., Bujarrabal, V., et al. 2021, A&A, 646, A1
Kamiński, T., Steffen, W., Tylenda, R., et al. 2018, A&A, 617, A129
Kamiński, T., Tylenda, R., Kiljan, A., et al. 2021, A&A, 655, A32
Kamiński, T., Tylenda, R., Menten, K. M., et al. 2018, Nature Astronomy, 2, 778
Karakas, A. I. & Lugaro, M. 2016, ApJ, 825, 26
Kato, T. 2003, A&A, 399, 695
Khouri, T., Vlemmings, W. H., Tafoya, D., et al. 2022, Nature Astronomy, 6, 275
Kimura, R. K., Gruenwald, R., & Aleman, I. 2012, A&A, 541, A112
Koller, J. & Kimeswenger, S. 2001, ApJ, 559, 419
Lau, R. M., Werner, M., Sahai, R., & Ressler, M. E. 2016, ApJ, 833, 115
Liu, N., Stephan, T., Boehnke, P., et al. 2017, ApJ, 844, L12
Lodders, K. 2003, ApJ, 591, 1220
Lumsden, S., Puxley, P., & Hoare, M. 2001a, MNRAS, 320, 83
Lumsden, S., Puxley, P., & Hoare, M. 2001b, MNRAS, 328, 419
Luridiana, V., Morisset, C., & Shaw, R. A. 2015, A&A, 573, A42
Mari, M. B., Akras, S., & Gonçalves, D. R. 2023, MNRAS, 525, 1998
Marigo, P. 2022, Universe, 8, 243
Metzger, B. D. & Pejcha, O. 2017, MNRAS, 471, 3200
Miller Bertolami, M. M. 2016, A&A, 588, A25
Miszalski, B., Boffin, H. M., & Corradi, R. L. 2012, MNRAS letters, 428, L39
Mobeen, M. Z., Kamiński, T., Matter, A., et al. 2024, A&A, 686, A260
Morisset, C., Delgado-Inglada, G., & Flores-Fajardo, N. 2015, Rev. Mexicana Astron. Astrofis., 51, 103
Nakashima, J.-i., Sobolev, A. M., Salii, S. V., et al. 2015, PASJ, 67
Nandez, J. L., Ivanova, N., & Lombardi Jr, J. C. 2014, ApJ, 786, 39
Osterbrock, D. E. & Ferland, G. J. 2006, Astrophysics Of Gas Nebulae and Active Galactic Nuclei (University science books)
Otsuka, M., Ueta, T., Van Hoof, P. A., et al. 2017, ApJS, 231, 22
Pejcha, O., Metzger, B. D., Tyles, J. G., & Tomida, K. 2017, ApJ, 850, 59
Perrott, Y. C., Scaife, A. M., Green, D. A., et al. 2015, MNRAS, 453, 1396
Pickett, H., Poynter, R., Cohen, E., et al. 1998, JQSRT, 60, 883
Preibisch, T., Ossenkopf, V., Yorke, H. W., & Henning, T. 1993, A&A, 279, 577
Pulliam, R., Edwards, J., & Ziurys, L. 2011, ApJ, 743, 36
Qiu, J.-J., Zhang, Y., Nakashima, J.-i., et al. 2023, A&A, 669, A121
Raga, A. C., Riera, A., Mellema, G., Esquivel, A., & Velázquez, P. 2008, A&A, 489, 1141
Sale, S. E., Drew, J. E., Barentsen, G., et al. 2014, MNRAS, 443, 2907
Sánchez Contreras, C., Bujarrabal, V., & Alcolea, J. 1997, A&A, 327, 689
Sánchez Contreras, C., Bujarrabal, V., Neri, R., & Alcolea, J. 2000, A&A, 357, 651
Sánchez Contreras, C., Velilla Prieto, L., Agúndez, M., et al. 2015, A&A, 577, A52
Schlegel, D. J., Finkbeiner, D. P., & Davis, M. 1998, ApJ, 500, 525
Schmidt, D. R., Woolf, N. J., Zega, T. J., & Ziurys, L. M. 2018, Nature, 564, 378
Schmidt, D. R. & Ziurys, L. M. 2016, ApJ, 817, 175
Schmidt, D. R. & Ziurys, L. M. 2017a, ApJ, 835, 79
Schmidt, D. R. & Ziurys, L. M. 2017b, ApJ, 850, 123
Schmidt, D. R. & Ziurys, L. M. 2019, ApJ, 881, L38
Shara, M. M. & Moffat, A. F. J. 1982, ApJ, 258, L41
Shara, M. M., Moffat, A. F. J., & Webbink, R. F. 1985, ApJ, 294, 271
Soker, N. & Tylenda, R. 2003, ApJ, 582, L105
Steinmetz, T., Kamiński, T., Schmidt, M., & Kiljan, A. 2024, A&A, 682, A127
Stephan, T., Trappitsch, R., Hoppe, P., et al. 2024, ApJS, 270, 27
Storey, P. J. & Hummer, D. G. 1995, MNRAS, 272, 41
Suárez, O., Gómez, J. F., & Miranda, L. F. 2008, AJ, 689, 430
Tafoya, D., Orosz, G., Vlemmings, W., Sahai, R., & Pérez-Sánchez, A. 2019, A&A, 629, A8
Tajitsu, A. & Tamura, S. 1998, AJ, 115, 1989
Toalá, J., Jiménez-Hernández, P., Rodríguez-González, J., et al. 2021, MNRAS, 503, 1543
Tylenda, R. 2005, A&A, 436, 1009
Tylenda, R., Hajduk, M., Kamiński, T., et al. 2011, A&A, 528, A114
Tylenda, R., Kamiński, T., & Mehner, A. 2019, A&A, 628, A124
Tylenda, R., Kamiński, T., & Smolec, R. 2024, A&A, 685, A49
Van de Steene, G., Van Hoof, P., Exter, K., et al. 2015, A&A, 574, A134
van de Steene, G. C. & Zijlstra, A. A. 1994, A&AS, 108, 485
Vastel, C., Bottinelli, S., Caux, E., Glorian, J. M., & Boiziot, M. 2015, in SF2A-2015: Proceedings of the Annual meeting of the French Society of A&A, 313
Ventura, P., Dell'Agli, F., Schneider, R., et al. 2014, MNRAS, 439, 977
Ventura, P., Dell'Agli, F., Lugaro, M., et al. 2020, A&A, 641, A103
Ventura, P., Tosi, S., García-Hernández, D., et al. 2025, A&A, 694, A177
Viironen, K., Greimel, R., Corradi, R. L., et al. 2009, A&A, 504, 291
Villaver, E., Manchado, A., & Garcia-Segura, G. 2002, ApJ, 581, 1204
Wannier, P. G., Andersson, B. G., Olofsson, H., Ukita, N., & Young, K. 1991, ApJ, 380, 593
Wen, S., Wang, Y.-Z., Hsia, C.-H., et al. 2024, A&A, 687, A99
Zhang, C. Y. 1995, ApJS, 98, 659
Zhang, Y., Liu, X.-W., Luo, S.-G., Péquignot, D., & Barlow, M. J. 2005, A&A, 442, 249
Zhukovska, S. & Henning, T. 2013, A&A, 555, A99

Appendix A: ALFOSC line fluxes

Table A.1: De-reddened integrated line fluxes from the ALFOSC spectrum taken on 08/12/2024.

Species	λ_{rest} (Å)	Core λ_{obs} (Å)	Core Flux/Hβ[a]	North λ_{obs} (Å)	North Flux/Hβ[a]	South λ_{obs} (Å)	South Flux/Hβ[a]
[Ne III]	3868.76	3870.01	1.46 ± 0.16	–	–	–	–
[S II]	4071.00	–	–	4069.95	0.60 ± 0.06	–	–
Hγ	4340.47	4340.99	0.64 ± 0.04	4341.59	0.55 ± 0.04	4339.74	0.37 ± 0.04
[O III]	4363.21	4363.28	0.39 ± 0.04	–	–	–	–
N I	4471.49	4472.59	0.18 ± 0.04	–	–	–	–
[S II]	4643.09	4642.65	0.13 ± 0.02	–	–	–	–
He II	4685.91	4685.22	0.30 ± 0.02	–	–	–	–
[O III]	4958.91	4957.63	3.83 ± 0.05	4961.11	0.13 ± 0.01	4959.54	0.43 ± 0.02
[O III]	5006.84	5005.47	11.74 ± 0.14	5008.90	0.44 ± 0.02	5006.60	1.02 ± 0.02
[N I]	5197.90	5197.24	0.11 ± 0.01	5198.83	4.64 ± 0.08	5196.52	2.65 ± 0.05
[N II]	5754.59	5753.47	0.27 ± 0.01	5754.88	0.29 ± 0.01	5752.31	0.25 ± 0.01
He I	5875.62	5874.64	0.26 ± 0.01	5876.17	0.05 ± 0.01	–	–
[O I]	6300.30	6298.91	0.15 ± 0.01	6300.00	2.23 ± 0.04	6297.97	1.37 ± 0.03
[S III]	6312.06	6310.80	0.05 ± 0.01	–	–	–	–
[O I]	6363.78	6362.77	0.05 ± 0.01	6364.39	0.74 ± 0.01	6361.42	0.43 ± 0.01
[N II]	6548.05	6546.66	1.42 ± 0.02	6548.34	2.45 ± 0.04	6545.82	2.03 ± 0.04
Hα	6562.79	6562.56	2.96 ± 0.04	6562.98	2.91 ± 0.05	6560.48	2.70 ± 0.05
[N II]	6583.45	6582.07	4.17 ± 0.05	6583.63	7.57 ± 0.13	6581.12	6.02 ± 0.11
He I	6678.15	6678.35	0.06 ± 0.01	–	–	–	–
[S II]	6716.43	6714.54	0.06 ± 0.01	6716.44	0.53 ± 0.01	6713.68	0.36 ± 0.01
[S II]	6730.80	6728.75	0.08 ± 0.01	6730.87	0.84 ± 0.01	6728.06	0.54 ± 0.01
[Ar V]?[b]	7005.87	7004.18	0.02 ± 0.01	–	–	–	–
He I	7065.19	7061.86	0.15 ± 0.01	–	–	–	–

[a] Fluxes are normalised to the Hβ flux (1.38×10^{-13} erg cm^{-2} s^{-1} Å^{-1}). Flux uncertainties are 1σ statistical errors from Gaussian line fitting, including errors of the fitted Hβ line.
[b] Lines marked with '?' denote tentative identifications.

Appendix B: SMA line fluxes

Table B.1: Identified molecular line properties from the SMA spectrum.

Line	Transition	Rest frequency (GHz)	LSR velocity (km s^{-1})	FWHM (km s^{-1})	Integrated flux (Jy km s^{-1})
H_2CO	3 (1, 3) – 2 (1,2)	211.2115	-20.82	51	10.20 ± 4.99
$^{13}CH_3CN$	12 (11) – 11 (11)	213.8886	-6.23	30	3.83 ± 3.00
$^{13}CH_3CN$	12 (9) – 11 (9)	214.0487	-34.57	32	4.75 ± 3.91
$^{13}C^{17}O$	2–1	214.5732	-19.40	26	12.09 ± 3.54
^{13}CN	N=2–1, J=$\frac{5}{2}$–$\frac{3}{2}$, F_1=2–1, F=1–1	217.2908	-28.67	37	16.13 ± 4.18
$HCC^{13}CN$	24 (23) – 23 (22)	217.4196	-22.65	51	15.16 ± 5.19
^{13}CN	N=2–1, J=$\frac{5}{2}$–$\frac{3}{2}$, F_1=3–2, F=4–3	217.4672	-23.94	28	12.46 ± 3.76
CN	N=2–1, J=$\frac{3}{2}$–$\frac{3}{2}$, F=$\frac{1}{2}$–$\frac{1}{2}$	226.2874	-24.21	26	3.13 ± 1.81
CN	N=2–1, J=$\frac{3}{2}$–$\frac{3}{2}$, F=$\frac{5}{2}$–$\frac{3}{2}$	226.3419	-27.50	76	11.95 ± 6.63
$HC^{13}CCN$	25–24	226.4542	-35.04	97	11.21 ± 7.11
CN	N=2–1, J=$\frac{3}{2}$–$\frac{1}{2}$, F=$\frac{3}{2}$–$\frac{5}{2}$	226.6596	-20.49	54	24.51 ± 4.93
CN	N=2–1, J=$\frac{5}{2}$–$\frac{3}{2}$, F=$\frac{3}{2}$–$\frac{5}{2}$	226.8759	-18.29	37	37.21 ± 4.03
HC_3N	25–24	227.4189	-19.72	53	11.43 ± 4.88
CO	2–1	230.538	-20.06	33	87.26 ± 3.38
$H^{13}CN$	3–2	259.0118	-20.31	38	66.91 ± 4.04
$H^{13}CO^+$	3–2	260.2553	-22.85	31	17.19 ± 3.86
$HN^{13}C$	3–2	261.2633	-21.40	28	15.34 ± 3.65
CCH	N=3–2, J=$\frac{7}{2}$–$\frac{5}{2}$, F=3–2	262.0064	-16.79	32	8.47 ± 3.89
$HC^{13}CCN$	29–28	262.6733	-23.88	71	10.15 ± 6.13
HC_3N	29–28	263.7923	-17.85	41	5.00 ±4.44

Appendix C: SMA moment maps

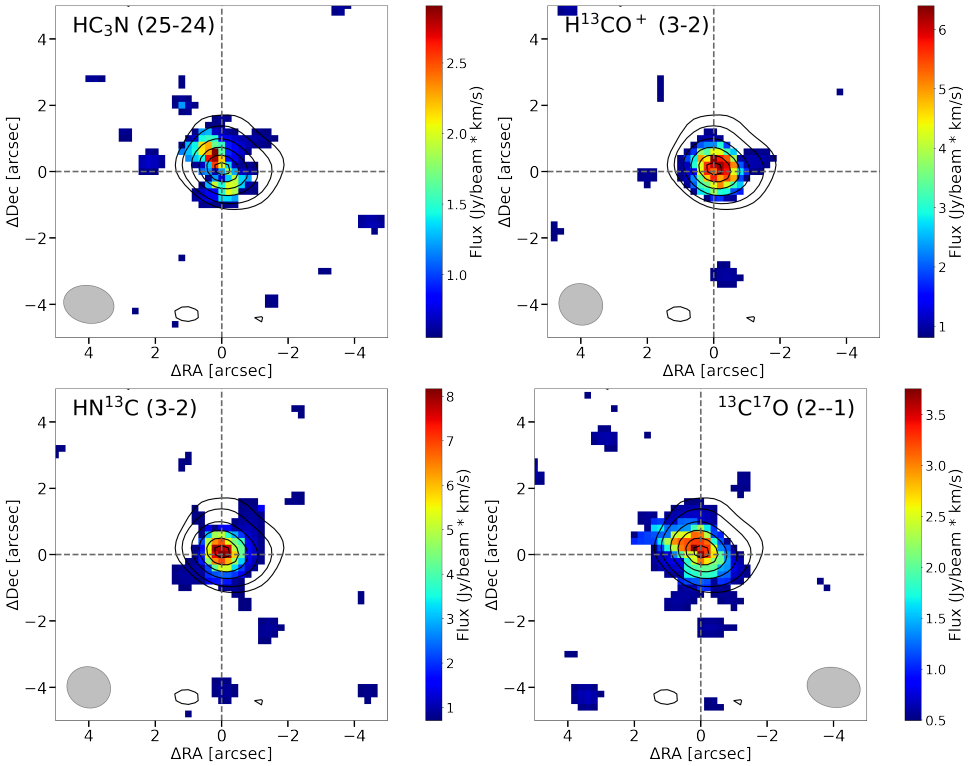

Fig. C.1: SMA 3σ integrated flux maps of HC_3N (25–24) (top left), $H^{13}CO^+$ (3–2) (top right), $HN^{13}C$ (3–2) (bottom left), and CN (bottom right). The contours are the same as for Fig. 6. The grey ellipse resembles the synthesised beam.

Appendix D: PV diagrams

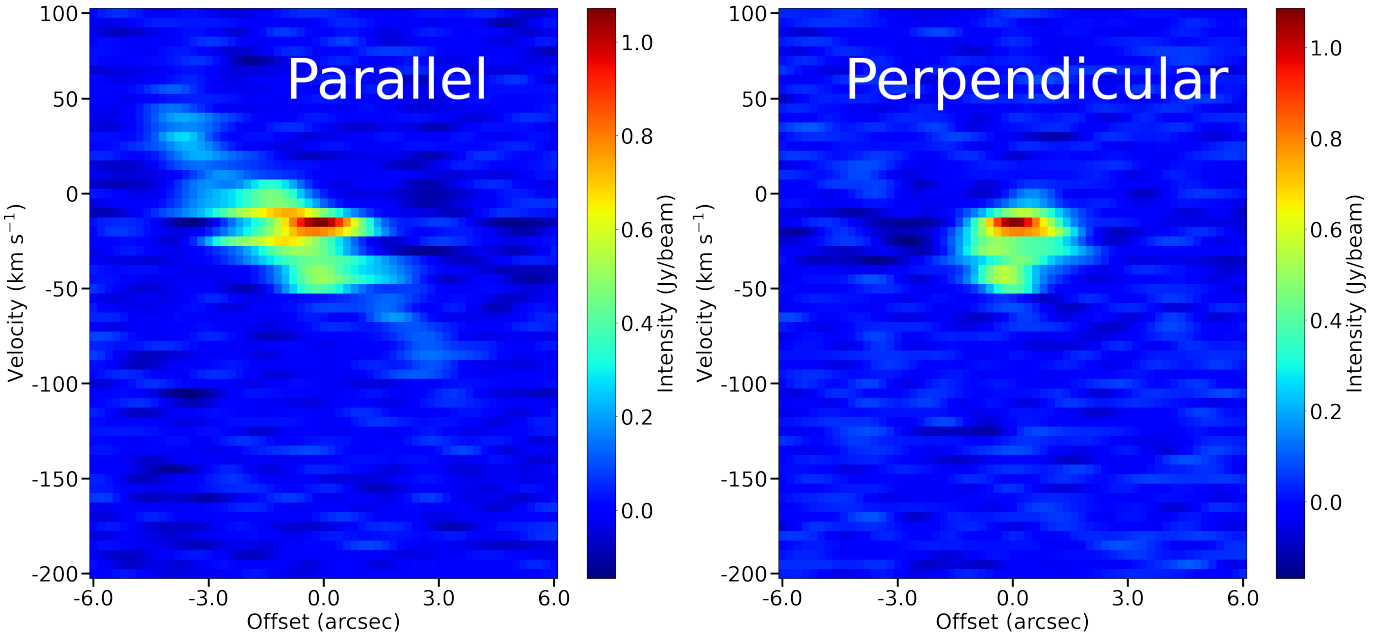

Fig. D.1: PV diagrams of the CO (2–1) emission, extracted at PA=41° (top panel) and 131° (bottom panel). The pixel width was 3 pixels, and the length of the PV extraction slit was 12″.

Appendix E: Interstellar reddening

In order to examine whether the reddening derived for K4-47 has a circumstellar contribution, we used the GALEXTIN VO service (Amôres et al. 2021) to extract estimated reddening values in the direction of K4-47 at different distances, using multiple different dust maps of the Galaxy. We utilised both dust models from Amôres & Lépine (2005), as well as the dust maps from Sale et al. (2014), and the Bayestar15,17,19 models (Green et al. 2015, 2018, 2019). Each dust map provides estimates of the interstellar extinction at a specified equatorial coordinate and at a specified distance. Using the various distance estimates of K4-47, including 3–7 kpc (Corradi et al. 2000), 5.9 kpc (Tajitsu & Tamura 1998), 8.5 kpc (Cahn et al. 1992), 20.42 kpc (Zhang 1995), and an upper limit of 26.5 kpc (van de Steene & Zijlstra 1994), we calculated values of E(B–V) for distance intervals of 0.1 kpc in the range of 3–26.5 kpc. We then convert A_V to E(B–V) using E(B–V)=A_V/R_V, and assuming R_V=3.1.

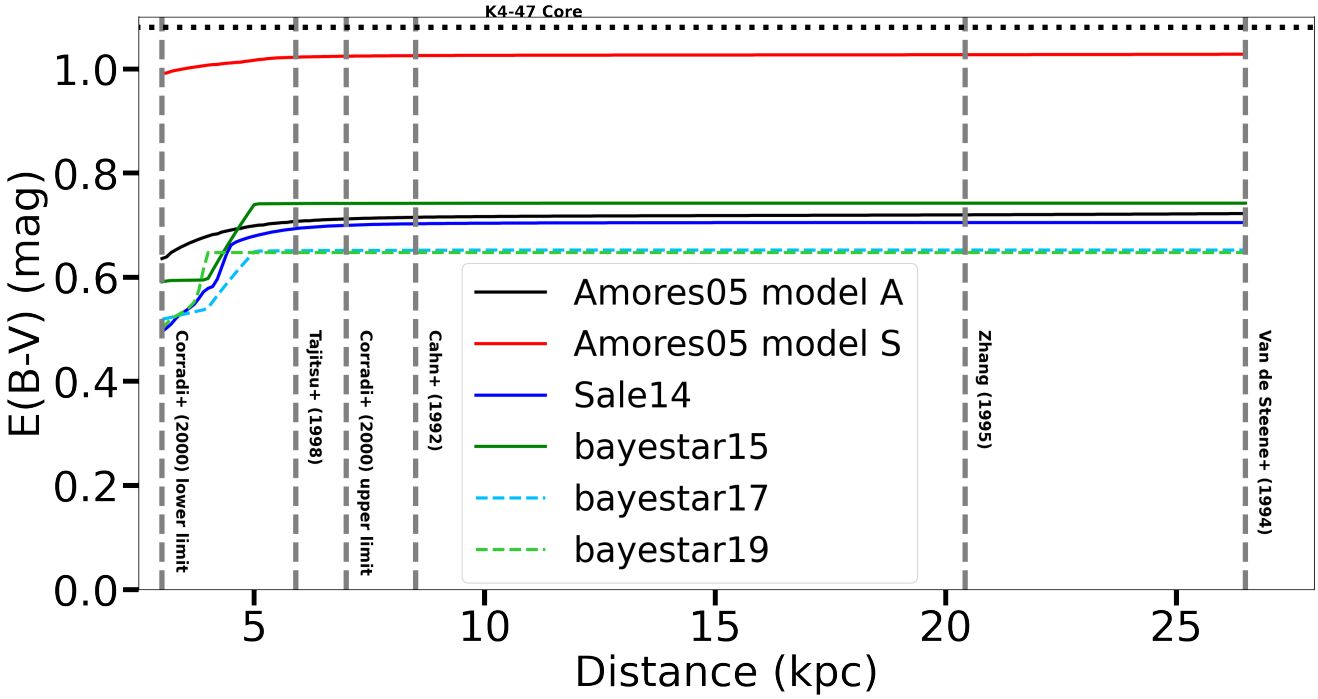

Fig. E.1: E(B–V) curves from the various models extracted via GALEXTIN. The dotted black line indicates the measured E(B–V) value for the core of K4-47, and dashed grey vertical lines indicate the estimated distances to K4-47 in the literature (references shown in the annotations).

We show the E(B–V) curves vs distance for each dust map in Fig. E.1. The majority of the outputs for each dust mass did not provide values in units of E(B–V). This was only true for the Bayestar15 model, which provides values for E(B–V) in the same units as Schlegel et al. (1998). For Bayestar17 and Bayestar19, we assume that these models are not equivalent to the units of Schlegel et al. (1998), meaning that output values of these models were multiplied by a factor of 0.996 to convert them to the desired units. Details of this conversion are provided via the Argonaut SkyMaps website[8]. Sale et al. (2014) provided extinction values in units of A_0, which is converted to A_V using the relation A_V=A_0/1.003.

[8] http://argonaut.skymaps.info/usage

Appendix F: SED fitting

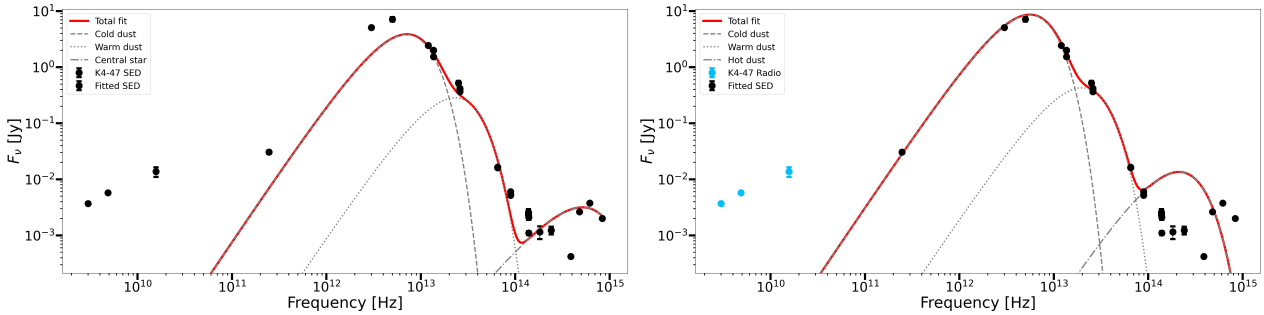

Fig. F.1: Modified blackbody fits to the full SED of K4-47. The left panel shows the fit to the 2-component dust + stellar blackbody, and the right panel shows the fit to the 3-component dust model. Dashed and dotted curves indicate the contribution from cold and warm dust, respectively, and the dash-dotted curves indicate the stellar flux in the left panel, and the hot dust in the right panel.

Appendix G: GALEX

K4-47 was covered by the GALEX survey on 02/01/2012 in two separate fields: AIS_53_0001_sg79 and AIS_53_0001_sg83. The data was observed with exposure times of 108 and 110 seconds, respectively, in the near-ultraviolet band ($\lambda_{\rm eff}$=2267 Å, $\lambda_{\rm FWHM}$=616 Å). We found no clear source within a 20″ aperture centred on the coordinates of K4-47 (α=04:20:45.263, δ=+56:18:12.44; see Fig. G.1). We calculated 5σ upper limits, where σ is derived from the root-mean-square (rms) noise within the aperture, for each frame and averaged them. The final averaged upper limit for K4-47 is 37.4 μJy at 2267 Å.

Within our Gaia archival maps, a source can be seen ∼30″ west of the location of K4-47 (Fig. G.1). To ensure that the astrometric solution of GALEX is sufficiently precise, so that we can be sure that this source is not in fact K4-47, we checked the Aladin Sky Atlas service[9] to look for nearby sources. A bright source (Gaia EDR3 276843597519980288: α=04:20:41.44, δ=+56:18:17.85) catalogued in the Gaia early release DR3 catalogue (Gaia Collaboration et al. 2021) is seen close to K4-47 and can be identified with the unrelated source found the GALEX maps. We show in Fig. G.1 a 10″ aperture centred on the Gaia source. We see that the aperture covers this source exactly, indicating this western source is not K4-47.

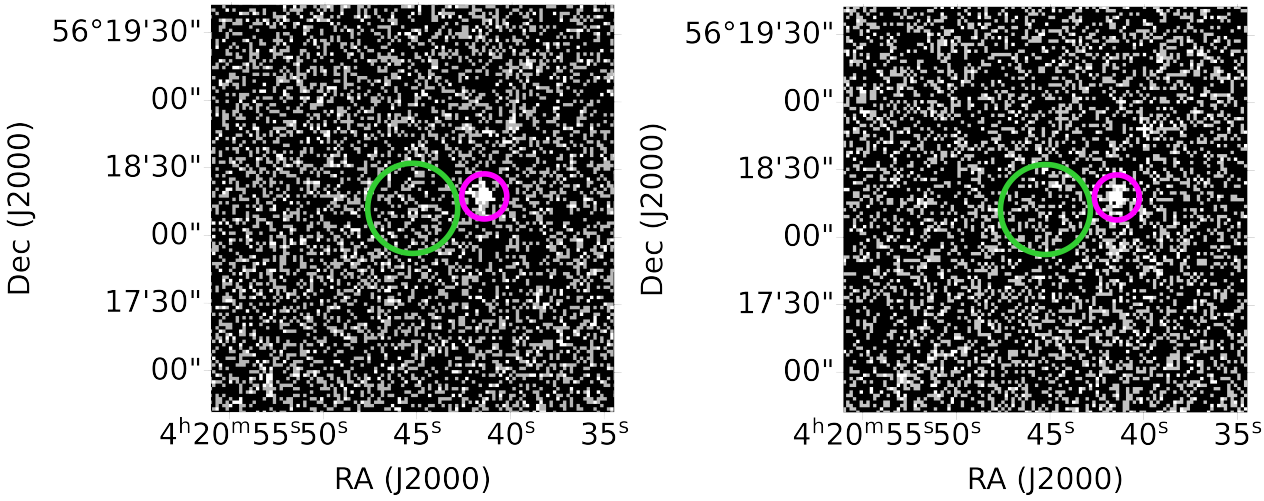

Fig. G.1: GALEX frames overlaid with a 20″ aperture (green) centred on the coordinates of K4-47. The magenta 10″ aperture is centred on the location of the nearby Gaia source.

[9] https://aladin.cds.unistra.fr/#Overview